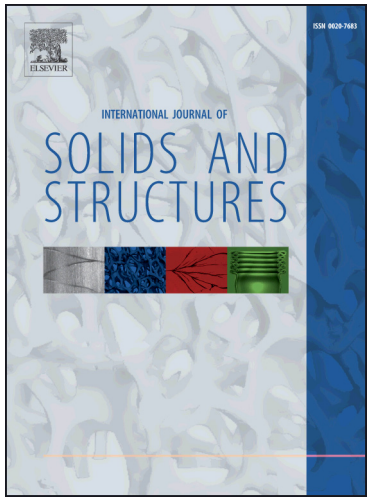

Effect of prestrains on swelling-induced buckling patterns in gel films with a square lattice of holes

Dai Okumura, Takahiro Inagaki, Nobutada Ohno

PII: S0020-7683(15)00025-6
DOI: http://dx.doi.org/10.1016/j.ijsolstr.2015.01.015
Reference: SAS 8626

To appear in: *International Journal of Solids and Structures*

Received Date: 2 July 2014
Revised Date: 26 December 2014

Please cite this article as: Okumura, D., Inagaki, T., Ohno, N., Effect of prestrains on swelling-induced buckling patterns in gel films with a square lattice of holes, *International Journal of Solids and Structures* (2015), doi: http://dx.doi.org/10.1016/j.ijsolstr.2015.01.015

Effect of prestrains on swelling-induced buckling patterns in gel films with a square lattice of holes

Dai Okumura [a,b,*], Takahiro Inagaki [b], Nobutada Ohno [a,b]

[a]Department of Mechanical Science and Engineering, Nagoya University, Furo-cho, Chikusa-ku, Nagoya 464-8603, Japan

[b]Department of Computational Science and Engineering, Nagoya University, Furo-cho, Chikusa-ku, Nagoya 464-8603, Japan

[*]Corresponding author. Tel.: +81 52 789 2671; fax: +81 52 789 4477.

E-mail address: okumura@mech.nagoya-u.ac.jp (D. Okumura)

Abstract:

We investigate the effect of prestrains on swelling-induced buckling patterns in polymeric films with a square lattice of holes. To reproduce experiments conducted by Zhang et al. (2008), poly(dimethylsiloxane) (PDMS) films are pre-strained in in-plane uniaxial tension in a lattice direction, and subsequently swelled by toluene. Finite element analysis is performed using an inhomogeneous field theory of polymeric gels in equilibrium, and with the aid of artificial damping. Periodic units consisting of 2×2 and 10×10 unit cells are analyzed under a generalized plane strain assumption. Analysis of the 10×10 unit cell shows that the resulting buckling pattern depends on the increase in prestrain of $\varepsilon = 0$, 0.2, 0.4 and 0.6, evolving as a diamond plate pattern ($\varepsilon = 0$), a slightly distorted diamond plate pattern ($\varepsilon = 0.2$), a binary pattern of circles and lines ($\varepsilon = 0.4$), and a monotonous pattern of ellipses ($\varepsilon = 0.6$). These predictions are in very good agreement with experiments. The 2×2 unit cell reveals that these different patterns appear continuously as transitional states during transformation into diamond plate patterns; prestrains in uniaxial tension delay the onset of the pattern transformation and equilibrium swelling interrupts the progress of the transformation. Parametric studies demonstrate that the pattern dependence on prestrains originates from intrinsic swelling features, and is a consequence of a particular combination of the selected polymer and solvent.

Keywords: Swelling, Gels, Buckling, Prestrains, Periodic structures, Finite element method.

1. Introduction

Swelling-induced instability creates a variety of complex and periodic wrinkle patterns in thin polymeric films (e.g., Tanaka et al., 1987; Guvendiren et al., 2009,2010; Breid and Crosby, 2009,2011; Li et al., 2012) and induces more complicated pattern transformation in thin polymeric films with periodic arrangements of holes (Zhang et al., 2008,2009; Singamaneni et al., 2009; Zhu et al., 2012). This instability and the resulting pattern transformation are spontaneously induced by in-plane compressive stress generated by the solvent swelling of thin polymeric films constrained on a substrate. Further, if films are subjected to prestrains prior to swelling, the resulting buckling patterns change depending on the type and amount of prestrain (Zhang et al., 2008,2009; Breid and Crosby, 2011). These complicated periodic patterns have wavelengths on the order of 0.1–10 μm and can form homogeneously over large regions depending on the size of the films. This property has allowed researchers to create complex patterns on nano- and microscales, switch photonic and phononic properties, tune surface adhesion and wetting, and develop nanoprinting methods (Zhang et al., 2008;2009; Jang et al., 2009; Yang et al., 2010; Zhu et al., 2012).

When thin polymeric films with a square lattice of circular holes are exposed to a solvent, a diamond plate pattern is typically observed in the absence of prestrains (Zhang el a., 2008; Singamaneni et al., 2009; Zhu et al., 2012). The square array of circular holes buckles and transforms into the diamond plate pattern, in which the circular holes are deformed into elliptical slits, and neighboring slits are arranged mutually perpendicular to each other. Zhang et al. (2008) observed the diamond plate pattern in poly(dimethylsiloxane) (PDMS) films using toluene as a solvent, and further investigated the effect of prestrains prior to solvent swelling on pattern transformation. In-plane uniaxial tension along a lattice direction was applied as prestrains, and

controlled by the nominal strain in that direction, ε (see Fig.1). They observed that the resulting buckling pattern varies continuously as the amount of prestrain ε is increased; the pattern evolves as a diamond plate pattern (ε = 0–0.1), a slightly distorted diamond plate pattern (ε = 0.2), a binary pattern of circles and lines (ε = 0.3–0.5), and a monotonous pattern of ellipses (ε = 0.5–0.8). Prestrains allow us to create and design a richer variety of periodic patterns from one polymeric film with a square lattice of circular holes.

The diamond plate pattern in the absence of prestrains has been analyzed in several studies. Zhang et al. (2008) and Matsumoto and Kamien (2009) used the linear elasticity theory to demonstrate that the diamond plate pattern minimizes the strain energy. They assumed that each hole collapses to a slit with an arbitrary orientation, and used the theory of cracks to model the slits as dislocation dipoles (Hirth and Lothe, 1982). In contrast, Hong et al. (2009) developed an inhomogeneous field theory of polymeric gels in equilibrium, and performed a finite element analysis of the diamond plate pattern to show the wide applicability of their theory. In their theory, the free-energy function of Flory and Rehner (1943) was applied to polymeric gels, and was implemented into the finite element software Abaqus using a user-defined subroutine UHYPER. They successfully reproduced the diamond plate pattern assuming a particular unit cell containing quarters of four neighboring holes (Hong et al., 2009; Ding et al., 2013). Okumura et al. (2014) also used this inhomogeneous field theory to analyze larger periodic units including random imperfections, and concluded that inhomogeneous imperfections play an important role in the homogeneous transformation into the diamond plate pattern. This inhomogeneous field theory is thus expected to allow analysis of the pattern dependence on prestrains, but such analyses have not yet been performed.

Zhang et al. (2008) pointed out that the dependence of buckling patterns on an amount of prestrain comes from the competition between tensile stress due to prestrains and compressive stress due to solvent swelling. Their paper did not describe a detailed mechanism, but this competition must disturb the equality of in-plane compressive stresses in two lattice directions induced by swelling. Prestrains may play a key role in determining the dominant buckling mode among many potential buckling modes, and such a change in the dominant buckling mode has been analyzed for hexagonal and square honeycombs under in-plane biaxial compression (Ohno et al., 2002,2004; Okumura et al., 2002,2004; Erami et al., 2006). However, for this possibility, the dominant buckling mode does not vary continuously as the amount of prestrain is increased, and it switches discontinuously depending on the ratio of in-plane biaxial compression. This possibility is not likely to give a reasonable explanation of the dominant buckling mode. A deeper understanding of the effect of prestrains may reveal an important factor which originates from mechanical and swelling properties of gels. It is thus interesting and worthwhile to investigate the effect of prestrains on swelling-induced buckling patterns in polymeric films with a square lattice of holes, and to elucidate the mechanism underlying the continuous change in buckling patterns as the prestrains increase in magnitude.

The present study investigates the effect of prestrains on the swelling-induced buckling patterns in gel films with a square lattice of holes. Finite element analysis is performed using the inhomogeneous field theory developed by Hong et al. (2009), which is briefly described in Section 2. Section 3 is devoted to numerical modeling. Periodic units including geometrical imperfections are analyzed, under a generalized plane strain assumption, with the aid of artificial damping. A set of boundary and loading conditions and a set of material parameters are determined in accordance with experiments (Zhang et al., 2008). Section 4 presents and interprets numerical results.

Predictions are shown to be in very good agreement with the experimental results, and thus, a reasonable explanation is given for the continuous change in buckling patterns with an increase in an amount of prestrain. In addition, in Section 5, parametric studies are performed to investigate the sensitivity of the resulting buckling patterns on material parameters. Finally, concluding remarks are given in Section 6.

2. Inhomogeneous field theory

This section briefly describes the inhomogeneous field theory of polymeric gels in equilibrium, which was developed by Hong et al. (2009). This theory considers that a polymer network is in contact with a solvent and subjected to mechanical loads and geometric constraints at a constant temperature. If the stress-free, dry network is taken as a reference state, the deformation gradient of the network is defined as $F_{ij} = \mathrm{d}x_i(\mathbf{X}) / \mathrm{d}X_j$, where X_j and $x_i(\mathbf{X})$ are the network coordinates of a gel system in reference and deformed states, respectively. When $C(\mathbf{X})$ is defined as the concentration of solvent molecules at a point in the gel system, the gel is in an equilibrium state characterized by the two fields $x_i(\mathbf{X})$ and $C(\mathbf{X})$. The free-energy density of the gel, W, is assumed to be a function of the deformation gradient, $\mathbf{F}$, and the concentration of solvent in the gel, C; i.e., $W(\mathbf{F},C)$. The inhomogeneous field theory may be applied to various free-energy functions for swelling elastomers, but this study uses the specific free-energy function of Flory and Rehner (1943). This is because this form is known to provide a basis for the interpretation of the swelling behavior of polymeric gels (Treloar, 1975), and has been demonstrated to reproduce the diamond plate pattern, as mentioned in Section 1 (Hong et al., 2009; Ding et al., 2013; Okumura et al., 2014).

The free-energy function of Flory and Rehner (1943) for a polymeric gel consists of

two terms associated with stretching and mixing of the free energies, and is written as

$$W = \frac{1}{2} NkT(I - 3 - 2\log J) - \frac{kT}{\upsilon}\left[\upsilon C \log\left(1 + \frac{1}{\upsilon C}\right) + \frac{\chi}{1 + \upsilon C}\right], \quad (1)$$

where $I = F_{ij}F_{ij}$ and $J = \det \mathbf{F}$ are invariants of the deformation gradient, N is the number of polymeric chains per reference volume, kT is the absolute temperature in the unit of energy, υ is the volume per solvent molecule, and χ is the Flory–Huggins interaction parameter that characterizes the enthalpy of mixing. As stated above, Eq. (1) takes an explicit form as a function of the deformation gradient, **F**, and the solvent concentration, C.

Considering δx_i and δC to be arbitrary variations of x_i and C, respectively, from a state of equilibrium, the virtual work principle gives an equilibrium equation in which the change of the free energy of the gel equals the sum of the work done by the external mechanical force and external solvent. That is,

$$\int_V \delta W dV = \int_V B_i \delta x_i dV + \int_A T_i \delta x_i dA + \mu \int_V \delta C dV\,, \quad (2)$$

where V is the reference volume and A is the reference surface. The first and second terms on the right-hand side are the mechanical work done by body forces and surface forces, respectively, and the third term represents the work done by the external solvent. Here, μ is the chemical potential of the external solvent, and is equivalent to that in the gel; that is,

$$\mu = \frac{\partial W}{\partial C}\,. \quad (3)$$

A Legendre transformation allows the free-energy function $W(\mathbf{F},C)$ to be transformed into another form (Hong et al., 2009),

$$\hat{W} = W - \mu C\,, \quad (4)$$

which is defined as a function of **F** and μ; i.e., $\hat{W}(\mathbf{F}, \mu)$. Combination of Eqs. (2) and (4) leads to

$$\int_V \delta \hat{W} dV = \int_V B_i \delta x_i dV + \int_A T_i \delta x_i dA . \quad (5)$$

When the gel is in a state of equilibrium, the chemical potential of the solvent molecules in the gel is homogeneous and equals the chemical potential of the external solvent, μ. Consequently, μ is regarded as a state variable, and the equilibrium condition (5) takes the same form as that for a hyperelastic solid.

Assuming that the network of polymers and pure liquid solvent are incompressible, the volume of the gel can be expressed as the sum of the volume of the dry network and that of the swelling solvent. This assumption leads to (Hong et al., 2009)

$$1 + \upsilon C = J . \quad (6)$$

Using Eqs. (1), (4) and (6), the Flory–Rehner free-energy function can be rewritten as

$$\hat{W} = \frac{1}{2} NkT(I - 3 - 2\log J) - \frac{kT}{\upsilon}\left[(J-1)\log\frac{J}{J-1} + \frac{\chi}{J}\right] - \frac{\mu}{\upsilon}(J-1) . \quad (7)$$

It is noted that the resulting free-energy function (7) takes an explicit form as a function of the deformation gradient, **F**, and the external chemical potential, μ. Eq. (7) acts as a free-energy function for a compressible hyperelastic material because of the volumetric change induced by solvent absorption. For example, the finite element package Abaqus offers a user-defined subroutine, UHYPER or UMAT, to implement the constitutive behavior of Eq. (7). The external chemical potential, μ, is passed into UHYPER or UMAT using the variable of temperature (Hong et al., 2009; Kang and Huang, 2010a). The concentration of the solvent molecules in the gel, *C*, is calculated from Eq. (6) after **F** is solved.

When the external solvent is subjected to pressure *p* under constant temperature, the solvent can be a gas or a liquid in equilibrium with its own vapor. Assuming the solvent to be incompressible in the liquid phase and to be an ideal gas in the gaseous phase, the chemical potential of the external solvent is expressed as

$$\mu = \begin{cases} (p - p_0)\upsilon & \text{if } p \geq p_0 \\ kT \log(p / p_0) & \text{if } p < p_0 \end{cases}, \tag{8}$$

where p_0 is the vapor pressure of the solvent (e.g., Hong et al., 2009; Kang and Huang, 2010a,b). The chemical potential is set to zero at the equilibrium vapor pressure ($p = p_0$), and the solvent is in an ideal gas phase if $p < p_0$ and an incompressible liquid phase if $p > p_0$. The chemical potential is $\mu = -\infty$ in a vacuum and $\mu = (p_{\text{atm}} - p_0)\upsilon$ at atmospheric pressure p_{atm} (=101 kPa).

It should be noted that the free-energy function (1) is singular when the network of polymers is in the dry state; i.e., when $\upsilon C = 0$. The right-hand side of Eq. (3) is also singular in the dry state and takes a value of negative infinity; i.e., $\mu = -\infty$. This relation is thus consistent with Eq. (8) in a vacuum, because the network of polymers in a vacuum cannot keep molecular solvents within the network and releases them to the vacuum. However, this singularity causes problems when numerical calculations include the dry state (Hong et al., 2009). Hong et al. (2009) introduced Eq. (7) into a user-defined subroutine UHYPER in Abaqus, and proposed a method to avoid this singularity. They assumed a free swelling state characterized by the homogeneous deformation gradient $F_{ij}^0 = \lambda_0 \delta_{ij}$, leading to $\upsilon C = \lambda_0^3 - 1 > 0$, as the reference state in numerical calculations (cf. Kang and Huang, 2010a). The stress of the reference state is homogeneously zero, and the finite value of the chemical potential of the reference state, μ_0, can be calculated analytically under these conditions. The employment of UHYPER can provide a quasi-dry state using a small deviation of λ_0 from 1, which is referred to as the reference state in this study.

In this study, the swelling process is reproduced by increasing the external chemical potential from a quasi-dry state ($\mu = \mu_0 < 0$) to an equilibrium swelling state ($\mu = 0$). The quasi-dry state is chosen as the reference state that avoids the above-mentioned

singularity, while the equilibrium swelling state is defined as the state in which the network of polymers is in contact with the liquid solvent ($p = p_0$). The differential pressure, $p_{\text{atm}} - p_0$, causes a negligible increase in the external chemical potential, which is estimated as $(p_{\text{atm}} - p_0)\upsilon / kT = 10^{-4} - 10^{-3}$ using representative values for solvents, $p_0 = 1 - 10$ kPa and $\upsilon = 10^{-29} - 10^{-28}$ m^3 , at room temperature, $kT = 4 \times 10^{-21}$ J . Hence, the effect of the atmospheric pressure can be ignored for the solvent (Wu et al., 2013). Further, this effect is expected to be small and negligible for the network of polymers, because polymers are generally regarded as stress-free at atmospheric pressure. Incidentally, Kang and Huang (2010b) discussed the effect of atmospheric pressure on swelling in a film constrained on a rigid substrate. More detailed analysis may need to consider atmospheric pressure (Kang and Huang, 2010b).

3. Numerical modeling

3.1. Generalized plane strain problem

Fig. 1 shows schematic diagrams in which a polymeric film with a square lattice of holes is first subjected to prestrains and then swelled by a solvent. In accord with experiments carried out by Zhang et al. (2008), in-plane uniaxial tension along a lattice direction is given as prestrains, and a controlled amount of nominal strain ε is retained during swelling subsequent to application of the prestrains. Swelling is caused by applying a liquid solvent on the polymeric film, and this application is assumed to be limited to the center region on the film surface, so that the swelling in this region is constrained by the surrounding region including lateral and bottom sides. Hence, the resulting in-plane compressive stress acts as a driving force to induce buckling and pattern transformation. Zhang et al. (2008) experimented with PDMS films using

toluene as a solvent, and observed the diamond plate pattern in the absence of prestrains under a wide range of conditions; hole diameter $d = 0.35 - 2\,\mu\text{m}$, pitch $l = 0.8 - 5\,\mu\text{m}$ and depth $h = 4 - 9\,\mu\text{m}$. They reported that this transformation occurs in the case of high aspect ratios of $h/d = 2 - 18$ and $l/d < 6$. Thus, the problem to be solved is 3-dimensional in reality (Singamaneni et al., 2009), but can be analyzed as a 2-dimensional problem using generalized plane strain elements in finite element analysis (Hong et al., 2009; Okumura et al., 2014). In this study, a type of generalized plane strain element, CPEG4H, is used in the Abaqus analysis. The dimensions of the gel film are reduced to *d* and *l*, and $d = 0.75\,\mu\text{m}$ and $l = 1.5\,\mu\text{m}$ are taken according to experiments conducted by Zhang et al. (2008) (see Fig.2).

3.2. Periodic units and imperfections

As reported in Zhang et al. (2008), pattern transformation occurs homogeneously over the entire sample with an area of up to 1 cm^2 with no random defects. In this case, a tremendous number of holes (about 44,000,000 holes when l = 1.5 μm) are in the sample. It is not reasonable to analyze the entire sample with the whole boundary conditions mentioned in Section 3.1. Hence, periodic units consisting of 10×10 and 2×2 unit cells are analyzed in this study. The periodic units were used by Okumura et al. (2014) to reproduce the diamond plate pattern in the absence of prestrains and to investigate the effect of inhomogeneous imperfections on the homogeneous transformation. Fig.2 shows the periodic units and their finite element meshes. The numbers of nodes and elements are 67,421 and 64,000, respectively, for the 10×10 unit cell (Fig. 2a), and are 2749 and 2560, respectively, for the 2×2 unit cell (Fig. 2b). Imperfections are introduced by considering each hole as a randomly oriented elliptical hole. Elliptical holes are defined using two parameters, α and θ. The parameter α represents the magnitude of imperfection, so that the major and minor diameters of an

elliptical hole are expressed as $d_{\mathrm{L}} = d(1+\alpha)$ and $d_{\mathrm{S}} = d(1-\alpha)$, respectively. The other parameter θ represents the angle between the major diameter and x_1 axis. If $\alpha = 0$, the hole is a perfect circle regardless of θ.

In the 10×10 unit cell (Fig. 2a), the angles θ_{ij} ($i = 1-10$, $j = 1-10$) are assigned to individual holes, and determined using random numbers. The set of θ_{ij} is not listed to avoid redundancy. For simplicity, α is fixed at 0.01 for all holes in this study. Scanning electron microscopy images (Zhang et al., 2008) imply that $\alpha = 0.01-0.05$ is a realistic range. Okumura et al. (2014) reported that large unit cells, such as 10×10 unit cells, are needed to investigate the effect of inhomogeneous imperfections on the homogeneous transformation into the diamond plate pattern in the absence of prestrains. However, they also showed that smaller unit cells, such as 2×2 unit cells, can reproduce the diamond plate pattern if imperfections are selected intentionally. In this study, the 2×2 unit cell (Fig. 2b) is used to make a more detailed analysis of results. The 2×2 unit cell includes three perfect circular holes and one elliptical hole characterized by $\alpha = 0.01$ and $\theta = 0°$.

It should be noted that large unit cells, such as 10×10 unit cells, are needed for analysis especially in the presence of prestrains, because it is unknown whether 2×2 unit cells express the dominant buckling patterns or not. However, it will be demonstrated in Section 4 that regardless of the presence of prestrains, both periodic units successfully reproduce the experimentally observed patterns.

3.3. Material parameters

Free-energy function (1) needs three material parameters, N, υ and χ, which are determined from experimental data recorded at room temperature and atmospheric

pressure. Initial Young's modulus E for the dry network of polymers is related to N by $kT = 4\times10^{-21}$ J and $E = 3NkT$ (e.g., Treloar, 1975). Experimental data show $E = 1-2$ MPa for PDMS made from mixing PDMS prepolymer and its curing agent at a weight ratio of 10:1 (Roca-Cusachs et al., 2005; Brown et al., 2005; Gupta et al., 2007; Degand et al., 2014). The density and molar mass for toluene then provide $\upsilon = 1.76\times10^{-28}$ m^3. Experiments (Chahal et al., 1973; Petri et al., 1995) show $\chi = 0.6-0.8$ for the system of PDMS and toluene. This value decreases from about 0.8 to about 0.6 as the volume fraction of toluene increases from 0 to about 0.5; χ decreases as PDMS swells in the presence of toluene. Detailed analyses need to consider this dependence (Huggins, 1964; Cai and Suo, 2011; Ding et al., 2013), but in this study, averaged values are used to investigate the effect of prestrains on buckling and pattern transformation in Section 4; i.e., $E = 1.5$ MPa and $\chi = 0.7$. The set of these material parameters can be confirmed by comparing the swelling ratio $S = D/D_0$ with the results of experiments carried out by Lee et al. (2003). Under free, isotropic swelling, D and D_0 are the lengths of PDMS in the solvent and of the dry PDMS, respectively. Using the set of selected material parameters, free-energy function (1) predicts $S = 1.30$ at equilibrium swelling ($\mu = 0$), which is consistent with an experimentally measured value of 1.31 (Lee et al., 2003). Parametric studies are performed in Section 5 to investigate the sensitivity of pattern transformation to selected material parameters.

3.4. Boundary and loading conditions

Periodic boundary conditions are imposed on the boundary of each periodic unit, and are expressed as (e.g., Bertoldi et al., 2008)

$$u_i^{(+)} - u_i^{(-)} = (\bar{F}_{ij} - \delta_{ij})(X_j^{(+)} - X_j^{(-)}) = \bar{H}_{ij}(X_j^{(+)} - X_j^{(-)}), \tag{9}$$

where $u_i^{(+)}$ and $u_i^{(-)}$ are the displacements at a point $X_j^{(+)}$ on the periodic unit boundary and the opposite point $X_j^{(-)}$, respectively, and the displacement is defined as $u_i = x_i - X_i$. In Eq. (9), $\bar{F}_{ij}$ and δ_{ij} denote the macroscopic deformation gradient and Kronecker delta, respectively, and thus $\bar{H}_{ij}$ denotes the macroscopic displacement gradient. The out-of-plane component $\bar{H}_{33}$ is determined using the generalized plane strain condition; i.e., using $\bar{S}_{33}$ =0, where $\bar{S}_{ij}$ denotes the macroscopic first Piola–Kirchhoff stress. Here, $\bar{F}_{ij}$, $\bar{H}_{ij}$ and $\bar{S}_{ij}$ are the macroscopic variables relative to the quasi-dry state, which is introduced using $\lambda_0 = 1.01$ (see Appendix A), resulting in $\mu_0 = -1.90kT$ (see Section 2). At this reference state ($\mu_0 = -1.90kT$), $\bar{F}_{ij}$, $\bar{H}_{ij}$ and $\bar{S}_{ij}$ are initialized as $\bar{F}_{ij} = \delta_{ij}$, $\bar{H}_{ij} = 0$ and $\bar{S}_{ij} = 0$. The macroscopic deformation gradient $\bar{H}_{ij}$ caused by one of the prestrains (ε = 0, 0.2, 0.4 and 0.6) is obtained assuming that in-plane uniaxial tension is expressed as $\bar{H}_{11} = \varepsilon$, $\bar{S}_{22} = 0$ and $\bar{H}_{ij} = 0\ (i \neq j)$; $\bar{H}_{22}$ is solved as an unknown value. Under the constraints of $\bar{H}_{11}(=\varepsilon)$ and $\bar{H}_{22}$, the swelling process is simulated by incrementally increasing μ from μ_0 to 0. Automatic time incrementation is used in the Abaqus analysis.

3.5. Artificial damping

Hong et al. (2009) and Okumura et al. (2014) reported that the problem to be solved here has snap-through instability at an unstable point, at which the iterative calculations for the next increment cannot be completed in the Abaqus analysis. The unstable point appears immediately after the onset of pattern transformation, and prevents the Abaqus analysis from progressing with further swelling. This unstable problem can be solved with the aid of artificial damping. The present study employs an automatic stabilization scheme with a constant damping factor, which is available in Abaqus using the STABILIZE option. Terms for viscos forces, which consist of an artificial mass matrix, a damping factor, the vector of nodal velocities and the increment of time, are added to

global equilibrium equations. The damping factor is automatically calculated from the dissipated energy fraction ω. This fraction ω should be increased if the iterative calculations are unstable and do not converge, while it should be decreased if the solution is unrealistic. The value of this fraction needs to be optimized by trial-and-error calculations, and is thus taken as $\omega = 2.5\times10^{-11}$ for the 10×10 unit cell and $\omega = 10^{-12}$ for the 2×2 unit cell (see Appendix B). Moreover, further swelling beyond unstable points can result in the self-contact of individual surfaces included in periodic units. Self-contact is considered in Abaqus analysis using the CONTACT INCLUSIONS option. Contacts are idealized as frictionless because the friction between contact surfaces is not expected to be a factor contributing to pattern transformation.

Incidentally, it may be generally known that eigenvalue buckling analysis (the BUCKLE option in Abaqus) and the arc-length method (the RIKS option in Abaqus) are helpful to analyze buckling modes and post-buckling behavior, respectively. However, in the present study, both options are not available with the inhomogeneous field theory. The BUCKLE option is based on a linear perturbation analysis procedure in Abaqus, so that temperature changes (i.e., chemical potential changes in the present study) are not active during eigenvalue buckling analysis. Similarly, the RIKS option is not implemented on the plane of chemical potential and displacement, as stated in Hong et al. (2009). Hence, the STABILIZE option, used in the present study, is useful for performing swelling-induced buckling analysis using the inhomogeneous field theory.

3.6. Deviation from roundness

To quantify the progress of pattern transformation in a deformed state, a measure of deviation from roundness is used for individual holes (Okumura et al., 2014). This

scalar value is zero when the hole is a perfect circle, and increases as the hole deviates from a perfect circle. The deviation from roundness is defined as

$$\Delta_{ij} = \min_{\mathbf{x}_{ij} \in \mathbf{x}} (r_{\max}(\mathbf{x}_{ij}) - r_{\min}(\mathbf{x}_{ij})) . \quad (10)$$

Here, $r_{\max}$ and $r_{\min}$ are the radii of circumscribed and inscribed circles of the hole identified by i and j in a periodic unit, respectively. Point $\mathbf{x}_{ij}$ is the center that minimizes the value $r_{\max} - r_{\min}$. To find the point $\mathbf{x}_{ij}$, trial calculations are performed at individual points on a square lattice with a 1-nm pitch. An elliptical hole with diameter d and imperfection magnitude α has $\Delta_{ij} = \alpha d$ in the initial undeformed state. For the 10×10 unit cell, $\Delta_{ij}\,(i = 1-10,\, j = 1-10)$ is estimated for 100 individual holes. Thus, $\bar{\Delta}$ is calculated as the average of all holes, and is used to interpret numerical results in the next section.

4. Results and discussion

4.1. Results for a 10×10 *unit cell*

Fig. 3 shows the macroscopic stress–strain relationships obtained for the 10×10 unit cell. Swelling due to solvent absorption increases the sum of in-plane compressive stress components normalized by NkT (i.e., $(\bar{S}_{11} + \bar{S}_{22}) / NkT$) and the out-of-plane tensile strain $\bar{H}_{33}$, although they are reduced by prestrains in uniaxial tension prior to swelling. Fig. 4 plots the macroscopic stress as a function of the deviation from roundness normalized by the representative diameter; i.e., $\bar{\Delta} / d$. The deviation from roundness is first increased depending on the amount of prestrain, because uniaxial tension deforms individual circular holes into elliptical holes with the major diameter in the loading direction. At the beginning of swelling, the deviation from roundness hardly

varies, and swelling contributes mainly to increasing the in-plane compressive stress, which acts as a driving force to induce buckling and the resulting pattern transformation. Figs. 3 and 4 clearly show that in two cases ($\varepsilon = 0$ and 0.2), pattern transformation starts when the in-plane compressive stress reaches the maximum stress, which is thus regarded as the initiation stress of pattern transformation. By contrast, the other two cases ($\varepsilon = 0.4$ and 0.6) do not have a maximum stress point. It is however noted that the corresponding curves indicate a slight pattern transformation around state (i) in Fig. 4, although this does not lead to a dramatic increase in $\bar{\Delta} / d$.

Figs. 5–8 show the deformed configurations for prestrains $\varepsilon = 0$, 0.2, 0.4 and 0.6, respectively. Each configuration is obtained from state (i), (ii), or (iii) represented in Fig. 4. Here, υC is a non-dimensional value of concentration C and represents the volumetric change due to solvent swelling (Eq. (6)). Fig. 5 shows that the absence of prestrain ($\varepsilon = 0$) predicts well the transformation into a diamond plate pattern. The pattern formation starts locally (Fig. 5a) and becomes homogeneous as $\bar{\Delta} / d$ increases (Fig. 5b). This increase terminates when all elliptical slits are perfectly closed, and subsequently, the compressive stress starts increasing again and continues to increase until swelling reaches equilibrium (Fig. 5c). Fig. 6 shows that the case of $\varepsilon = 0.2$ also predicts a local initiation of pattern transformation (Fig. 6a). The resulting pattern is not a diamond plate pattern but a binary pattern of circles and slits (Fig. 6b). Further swelling changes this binary pattern into a distorted diamond plate pattern (Fig. 6c). In contrast, although the other two cases ($\varepsilon = 0.4$ and 0.6) have a slight indication of pattern transformation around state (i) represented in Fig. 4, Figs. 7a and 8a show no initiation of pattern transformation; all holes are deformed as almost uniform ellipses by prestrains prior to swelling. However, further swelling until equilibrium swelling leads to different consequences that during the period between states (i) and (ii), the case of $\varepsilon = 0.4$ predicts transformation into a binary pattern of circles and slits (Fig. 7b), while

the case of $\varepsilon = 0.6$ predicts no pattern transformation; i.e., a monotonous pattern of ellipses (Fig. 8b).

Results obtained for the 10×10 unit cell agree well with the results of experiments carried out by Zhang et al. (2008). Swelling-induced buckling causes the homogeneous transformation into a diamond plate pattern ($\varepsilon = 0$–0.1), a distorted diamond plate pattern ($\varepsilon = 0.2$), a binary pattern of circles and slits ($\varepsilon = 0.3$–0.5), and a monotonous pattern of ellipses ($\varepsilon = 0.5$–0.8). This agreement supports the validity of the analytical conditions described in Section 3. The introduction of artificial damping (see Section 3 and Appendix B) allows us to analyze further swelling beyond the unstable points that appear immediately after the maximum stress point (cf. Okumura et al., 2014). It is found from Figs. 4 and 5 that in the absence of prestrains, the diamond plate pattern formation starts locally and becomes homogeneous during the period that the compressive stress decreases slightly from the maximum point. Figs. 4 and 8 show that the monotonous pattern of ellipses appears as a consequence of no pattern transformation when there is a large amount of prestrain; i.e., $\varepsilon = 0.6$. It should then be noted that further analysis and discussion are needed to give a reasonable explanation for the appearance of the distorted diamond plate pattern subsequent to the binary pattern of circles and slits in the case of $\varepsilon = 0.2$, and pattern transformation without the maximum stress point in the case of $\varepsilon = 0.4$.

Figs. 5–8 show that the resulting patterns have the periodicity of 2×2 unit cells regardless of the presence of prestrains, and long wave-length buckling, which depends on the size of periodic units (e.g., Ohno et al., 2004), does not occur. To obtain a detailed understanding of a series of pattern transformations, results of the 2×2 unit cell are presented in the next subsection.

4.2. Results for a 2×2 *unit cell*

Results obtained for the 2×2 unit cell are shown in Figs. 9 and 10. In Fig. 9, the average deviation from roundness is not used and the individual values for four holes, namely Δ_{11}, Δ_{12}, Δ_{21} and Δ_{22}, are plotted to obtain detailed traces of pattern formation. Fig. 10 shows the deformed configurations at states (i)–(iv) in Fig. 9. Although the 2×2 unit cell is smaller than the 10×10 unit cell, and includes only the imperfection of one hole (see Subsection 3.2), Fig. 10 indicates that this small unit cell successfully reproduces the specific formation processes predicted in the analysis of 10×10 unit cell (Figs. 5–8).

Fig. 10a shows the progress of transformation into a diamond plate pattern in the absence of prestrain ($\varepsilon=0$). This transformation deforms four circular holes into elliptic slits, which are arranged mutually perpendicular to each other (Fig. 10a); holes 11 and 22 have major diameters in the x_1 direction while holes 12 and 21 have major diameters in the x_2 direction. Four independent curves in Fig. 9a show almost the same profile, and hence, this profile is similar to that of the average deviation from roundness obtained for the 10×10 unit cell in Fig. 4. It is however found from Fig. 9b–d that the presence of prestrains diversifies the individual profiles, which cannot be represented by the average deviation from roundness (cf. Fig. 4).

Fig. 10b shows the progress of pattern transformation in the case of $\varepsilon=0.2$. A binary pattern with circles and slits appears at an intermediate state (state (iii)), followed by a distorted diamond plate pattern at equilibrium swelling (state (iv)). Fig. 9b clarifies the mechanism of this characteristic transformation. First, the prestrain deforms four circular holes into ellipses with the major diameter in the x_1 direction. When the process of sequential swelling induces transformation (state (ii)), holes 11 and 22 become more

elliptical in the same direction, thus being perfectly closed before arriving at equilibrium swelling, while holes 12 and 21 first revert from ellipses to circles (state (iii)) and subsequently deform into elliptical slits with the major diameter in a different direction; i.e., the x_2 direction. This means that transformation into a diamond plate pattern takes place regardless of the presence of the prestrain ($\varepsilon = 0.2$), and the prestrain assists the pattern formation of holes 11 and 22 while hindering that of holes 12 and 21. This difference produces a binary pattern with circles and slits, and thus a distorted diamond plate pattern. If further swelling is allowed beyond equilibrium swelling, all holes will finally close, and a diamond plate pattern will form with different pitches in the x_1 and x_2 directions (see Section 5).

The appearance of the binary pattern with circles and slits in the case of $\varepsilon = 0.4$ is explained by the mechanism described in the case of $\varepsilon = 0.2$. Figs. 9c and 10c show that there is also transformation into a diamond plate pattern in the case of $\varepsilon = 0.4$. Pattern transformation starts when the in-plane compressive stress reaches the maximum stress (state (ii)). Holes 11 and 22 become more elliptic while holes 12 and 21 tend to revert to circles. If further swelling is allowed, the pattern transformation progresses, resulting in a distorted diamond plate pattern, as shown in Fig. 10b, and finally a diamond plate pattern with different pitches in the x_1 and x_2 directions. However, equilibrium swelling causes this transformation to shut down. Thus, the binary pattern appears as a transitional state during transformation into the diamond plate pattern. It is thus found that equilibrium swelling plays an important role in interrupting the progress of the pattern transformation, and that this interruption diversifies the resulting swelling-induced buckling patterns. Incidentally, Fig. 9c clearly shows the initiation and progression of the pattern transformation. This progression dramatically increases and decreases the deviation from roundness for individual holes 11, 12, 21 and 22. Consequently, the average deviation from roundness possibly fails to

show the pattern transformation and its progress, as in the analysis of 10×10 unit cell (Fig. 4).

Fig. 10d shows no pattern transformation in the case of $\varepsilon=0.6$, resulting in a monotonous pattern of ellipses at equilibrium swelling. Hence, the values of the deviation from roundness for the four holes do not change dramatically after the prestrain is applied (Fig. 9d). Here, one may be interested in the quick increase and decrease among states (ii)–(iv). Figs. 9d and 10d show that the first change between states (ii) and (iii) is the transformation of elliptical holes 11 and 22 into lipped shapes, and subsequently, the other two elliptical holes transform into lipped holes between states (iii) and (iv). Consequently, the monotonous pattern of ellipses consists of lipped holes at equilibrium swelling. Transformation into the diamond plate pattern, which occurs for $\varepsilon=0$, 0.2 and 0.4, does not occur for $\varepsilon=0.6$. This transformation of all holes into lipped holes is confirmed by the 10×10 unit cell analysis, if careful attention is paid to Fig. 8, and the lipped holes can be found in the monotonous pattern of ellipses observed in experiments (Zhang et al., 2008).

Fig. 11 plots the in-plane compressive stress as a function of the external chemical potential. Fig. 11a shows the curves in the range from the quasi-dry state to the equilibrium swelling state, while Fig. 11b shows the curves enlarged around equilibrium swelling. It is found that an increase in an amount of prestrain delays the appearance of the maximum stress point (i.e., the initiation of pattern transformation) or prevents its appearance especially for a much larger amount of prestrain. This is because the prestrains decrease the in-plane compressive stress, and additional solvent absorption is generally needed to increase the in-plane compressive stress. This delay acts to prevent pattern transformation from taking place or to reduce swelling during transformation into a diamond plate pattern, leading to the appearance of a distorted diamond plate

pattern, a binary pattern with circles and slits, and a monotonous pattern of ellipses.

Incidentally, it is known that the total amount of swelling in equilibrium is increased by internal stress in tension but reduced by internal stress in compression (Treloar, 1975). This effect, which is implicitly introduced in the inhomogeneous field theory (Hong et al., 2009), is demonstrated by the concentration distributions in Figs. 5–8 and 10. The concentration difference in the unit cells becomes more remarkable particularly after pattern transformation. It may be worthwhile to discuss the possibility that uniaxial tension as prestrains increases the total amount of swelling in equilibrium, and thus promotes the progress of pattern transformation. However, in the present study, the uniaxial tension decreases the in-plane compressive stress that is a driving force to induce pattern transformation. It should be noted that, in general, swelling-induced instability phenomena can become a more complex combination of the above-mentioned negative and positive effects.

5. Parametric studies

Section 4 was devoted to explaining the mechanism by which the resulting swelling-induced patterns change continuously depending on an increase in prestrain ε; i.e., an increase in uniaxial tension prior to swelling. This mechanism implies that the resulting swelling-induced patterns are considerably sensitive to changes in the set of material parameters. Hence, this section investigates the pattern sensitivity to possible changes in material parameters.

As described in Subsection 3.3, the uncertainty in selected material parameters for the system of PDMS and toluene exists in Young's modulus E and the Flory–Huggins

interaction parameter χ, although E = 1.5 MPa and χ = 0.7 were used as average values in Section 4. Considering experimental data, the possibilities of E = 1–2 MPa and χ = 0.6–0.8 are considered here. It should be noted that these changes contribute mainly to the total number of toluene molecules that are absorbed in PDMS at equilibrium swelling. An increase in the two parameters has a tendency to decrease the total amount of swelling, while a decrease in the two parameters leads to an increase in the total amount of swelling (Treloar, 1975). Thus, the two cases are additionally analyzed as extreme situations: E = 2 MPa and χ = 0.8 as Case 1, and E = 1 MPa and χ = 0.6 as Case 3. Results of Case 2 (E = 1.5 MPa and χ = 0.7) are those presented in Section 4.

Fig. 12 shows the deformed configurations at equilibrium swelling in Cases 1, 2 and 3. In Case 1, a diamond plate pattern is predicted only in the absence of prestrain (ε = 0), and monotonous patterns of ellipses are predicted in the presence of prestrains (ε = 0.2, 0.4 and 0.6). This means that the set of material parameters cannot provide sufficient swelling for the transformation into the diamond plate pattern in the presence of prestrains. In Case 3, pattern transformation is predicted regardless of the presence of prestrains. This set of material parameters provides additional swelling compared with Cases 1 and 2. Diamond plate patterns appear when ε = 0.2 and ε = 0, while transitional patterns, which are similar to the distorted diamond plate pattern and the binary pattern with circles and slits, appear when ε = 0.4 and even when ε = 0.6. The results of Cases 1 and 3 show that the predictions are very sensitive to the set of selected material parameters.

These results indicate that if there is sufficient swelling, transformation into a diamond plate pattern is possible regardless of the amount of prestrain. However, the amount of swelling is restricted by equilibrium swelling. It is thus demonstrated that the

dependence of the pattern formation on prestrains (Zhang et al., 2008) is a consequence of a particular combination of the selected polymer and solvent; i.e., PDMS and toluene. Different organic solvents, such as acetone, ethyl alcohol, pentane and chloroform, can be used instead of toluene, where acetone and ethyl alcohol are poorer solvents than toluene for PDMS and pentane and chloroform are better solvents than toluene (Lee et al., 2003). The use of poor solvents is expected to result in no pattern transformation even in the absence of prestrain, while that of good solvents is expected to result in the diamond plate pattern even for larger prestrains. It is concluded from this discussion that the pattern formation due to swelling-induced buckling depends considerably on intrinsic swelling properties; i.e., swelling proceeds spontaneously but is interrupted by equilibrium swelling.

6. Concluding remarks

In this study, we investigated the effect of prestrains on the swelling induced buckling patterns in gel films with a square lattice of holes. The inhomogeneous field theory for polymeric gels developed by Hong et al. (2009) was used in finite element analysis. Periodic units consisting of 2×2 and 10×10 unit cells were analyzed under a generalized plane strain assumption. The swelling process was simulated by increasing the external chemical potential from a quasi-dry state to an equilibrium swelling state. Material parameters were determined from several experimental data for PDMS and toluene, and geometrical imperfections were introduced employing the approach used by Okumura et al. (2014). In addition, artificial damping was employed in further analysis beyond unstable points. The main findings of this study are as follows.

Analysis results of the 10×10 unit cell were in very good agreement with the results of experiments carried out by Zhang et al. (2008). The diamond plate pattern appears in the absence of prestrain, while the distorted diamond plate pattern, the binary pattern with circles and slits and the monotonous pattern of ellipses appear as the amount of prestrain (i.e., uniaxial tension prior to swelling) is increased. Analysis of the 2×2 unit cell revealed that the resulting different patterns appear continuously as transitional states during transformation into diamond plate patterns. Transformation into diamond plate patterns occurs regardless of the presence of prestrains, but an increase in prestrain delays the onset of this pattern transformation. This delay limits swelling during transformation because the total amount of swelling is restricted by equilibrium swelling; i.e., a combination of polymer and solvent. As a result, the distorted diamond plate pattern and the binary pattern with circles and slits form depending sensitively on the amount of prestrain. A sufficiently large amount of prestrain prevents pattern transformation, leading to the monotonous pattern of ellipses. Thus, parametric studies clarified that the appearance of transitional states in the presence of prestrains is a consequence of a particular combination of the selected polymer and solvent.

The above-mentioned findings revealed that the key factor in diversifying the resulting swelling-induced patterns in gel films with a square lattice of holes originates from intrinsic swelling properties; i.e., swelling proceeds spontaneously but is interrupted by equilibrium swelling. This mechanism may give a reasonable explanation for a variety of complex and periodic wrinkle patterns in gel films (Breid and Crosby, 2009,2011; Guvendiren et al., 2009,2010; Cai et al., 2011). Hence, inhomogeneous field theories for polymeric gels are expected to play an important role in analyzing these problems. From an experimental point of view, this approach can be used to predict resulting patterns that depend sensitively on material properties, dimensions of films,

and the kind of prestrain and its magnitude. Although experiments (Zhang et al., 2008) were successfully reproduced by analyzing periodic units with periodic boundary conditions, the entire films may be needed to be analyzed with the whole boundary conditions if a sufficient number of holes are not in the film (cf. Zhang et al., 2008). From a theoretical point of view, it may be interesting to discuss differences in the predictions made using more advanced free-energy functions based on phenomenological theories (e.g., Treloar, 1975; Boyce and Arruda, 2001; Bitoh et al., 2010; Drozdov and Christiansen, 2013) and more advanced inhomogeneous field theories that account for diffusion and temperature dependency (e.g., Hong et al., 2008; Chester and Anand, 2010; Cai and Suo, 2011; Ding et al., 2013). It may be especially interesting to investigate whether different buckling paths appear or not, and whether creasing occurs prior to buckling (Cai et al., 2010), when transient swelling process is considered in analysis. This investigation can be performed by the finite element analysis based on the inhomogeneous field theories that introduce the diffusion of solvent molecules (Toh et al., 2013, Chester et al., 2015) instead of assuming the quasi-static state (cf. Hong et al., 2009).

Acknowledgements

This research was supported by the Japan Society for the Promotion of Science (JSPS) under a Grant-in-Aid for Scientific Research (C).

Appendix A. Dependence on swelling ratio at quasi-dry state

As described in Section 2, the quasi-dry state is introduced to avoid singularity at the dry state in Abaqus analysis. In experiments by Zhang et al. (2008), PDMS films do not include toluene at the initial state, so that the swelling ratio at the quasi-dry state, λ_0, should be determined by considering a sufficiently small deviation from 1. The employment of sufficiently small deviations is expected to give no effect on the results, while the employment of larger deviations can produce results different from those obtained using the sufficient small deviations.

Fig. 13 shows the dependence of the resulting patterns at equilibrium swelling on the swelling ratio at the quasi-dry state. Two additional cases are used for 2×2 unit cell analysis (λ_0 =1.01 is the representative value in the present study); λ_0 =1.001 as a smaller case and λ_0 =1.1 as a larger case. The employments of λ_0 =1.001 and 1.01 predict the same pattern transformation depending on the amount of prestrains. Although the minimum and maximum values in the concentration distributions are not perfectly identical, the agreement is satisfactory for the predicted patterns. This means that λ_0 =1.01, used in the present study, is sufficiently small to reproduce the quasi-dry state. In contrast, Fig. 13 also shows that λ_0 =1.1 is too large to produce the results obtained using λ_0 =1.001 and 1.01. The deviation of λ_0 =1.1 from 1 may be small, but, in fact, is relatively large for the system of PDMS and toluene, because the swelling ratio in equilibrium under free, isotropic swelling is 1.31 (see Section 3.3). This relatively large deviation underestimates the in-plane compressive stresses due to swelling, resulting in no pattern transformation especially in the presence of prestrains (Fig. 13). These results indicate the importance to introduce the sufficiently small deviation of λ_0 from 1 to reproduce the quasi-dry state. In the different point of view,

the results also imply the importance to consider the swelling ratio at the initial state if a considerable amount of solvents is included in films at the initial state.

Appendix B. Dependence on artificial damping

As described in Subsection 3.5, the problem to be solved in the present study can have snap-though instability at an unstable point (Hong et al., 2009), and unstable points appear immediately after the onset of pattern transformation (Okumura et al., 2014). To continue the Abaqus analysis beyond unstable points, artificial damping is introduced using the STABILIZE option. Terms of viscos forces, which consist of an artificial mass matrix, a damping factor, the vector of nodal velocities and the increment of time, are added to global equilibrium equations. The damping factor is automatically calculated from a dissipated energy fraction ω.

Fig. 14 shows the maximum stress (i.e., the initiation stress of pattern transformation) as a function of prestrain for the analysis of 2×2 unit cell (see. Figs. 9 and 11). Five different curves are obtained using different values of the dissipated energy fraction ($\omega = 10^{-10}$, 10^{-11}, 10^{-12}, 10^{-13} and 0). Here, $\omega = 0$ means that there is no artificial damping. The figure shows that an increase in ω has a tendency to overestimate the initiation stress, while a decrease in ω results in a good prediction of the initiation stress obtained without artificial damping. Because of the nature of artificial damping, an excess decrease in ω prevents the iterative calculations in the Abaqus from being stable beyond unstable points. It is hence found from Fig. 14 that a value of ω should be selected in the range of approximately 10^{-11}–10^{-12} to obtain reasonable results. The present study employs $\omega = 10^{-12}$ for the 2×2 unit cell analysis, and $\omega = 2.5\times10^{-11}$ for the 10×10 unit cell analysis.

It is noted that a somewhat large value of ω is used for the 10×10 unit cell analysis. When $\omega = 10^{-12}$ is used for the analysis, the iterative calculations in Abaqus require a long computational time, and the analysis is not expected to be completed in reasonable time. This problem becomes serious especially when a number of individual holes start to self-contact with the progress of pattern transformation. Although the use of $\omega = 2.5\times10^{-11}$ overestimates the initiation stress slightly (Fig. 14), it should be emphasized that this slight overestimation does not affect the findings and conclusions of the present study (see Section 6).

References

Bertoldi, K., Boyce, M.C., Deschanel, S., Prange, S.M., Mullin, T., 2008. Mechanics of deformation-triggered pattern transformations and superelastic behavior in periodic elastomeric structures. J. Mech. Phys. Solids 56, 2642–2668.

Bitoh, Y., Akuzawa, N., Urayama, K., Takigawa, T., 2010. Strain energy function of swollen polybutadiene elastomers studied by general biaxial strain testing. J. Poly. Sci. B 48, 721–728.

Boyce, M.C., Arruda, E.M., 2001. Swelling and mechanical stretching of elastomeric materials. Math. Mech. Solids 6, 641–659.

Breid, D., Crosby, A.J., 2009. Surface wrinkling behavior of finite circular plates. Soft Matter 5, 425–431.

Breid, D., Crosby, A.J., 2011. Effect of stress state on wrinkle morphology. Soft Matter 7, 4490–4496.

Brown, X.Q., Ookawa, K., Wong, J.Y., 2005. Evaluation of polydimethylsiloxane scaffolds with physiologically-relevant elastic moduli: interplay of substrate mechanics and surface chemistry effects on vascular smooth muscle cell response.

Biomaterials 26, 3123–3129.

Cai, S., Bertoldi, K., Wang, H., Suo, Z., 2010. Osmotic collapse of a void in an elastomer: breathing, buckling and creasing. Soft Matter 6, 5770–5777.

Cai, S., Breid, D., Crosby, A.J., Suo, Z., Hutchinson, J.W., 2011. Periodic patterns and energy states of buckles films on compliant substrates. J. Mech. Phys. Solids 59, 1094–1114.

Cai, S., Suo, Z., 2011. Mechanics and chemical thermodynamics of phase transition in temperature-sensitive hydrogels. J. Mech. Phys. Solids 59, 2259–2278.

Chahal, R.S., Kao, W.P., Patterson, D., 1973. Thermodynamics of polydimethylsiloxane solutions. J. Chem. Soc., Faraday Trans. I, 69, 1834–1848.

Chester, S.A., Anand, L., 2010. A coupled theory of fluid permeation and large deformations for elastomeric materials. J. Mech. Phys. Solids 58, 1879–1906.

Chester, S.A., Di Leo, C.V., Anand, L., 2015. A finite element implementation of a coupled diffusion-deformation theory for elastomeric gels. Int. J. Solids Struct. 52, 1–18.

Degand, S., Knoops, B., Dupont-Gillain, C.C., 2014. Design and characterization of surfaces presenting mechanical nanoheterogeneities for a better control of cell-material interactions. Colloids Surf. A 442, 164–172.

Ding, Z.W., Liu, Z.S., Hu, J.Y., Swaddiwudhipong, S., Yang, Z.Z., 2013. Inhomogeneous large deformation study of temperature-sensitive hydrogel. Int. J. Solids Struct. 50, 2610–2619.

Drozdov, A.D., Christiansen, J.deC., 2013. Constitutive equations in finite elasticity of swollen elastomers. Int. J. Solids Struct. 50, 1494–1504.

Erami, K., Ohno, N., Okumura, D., 2006. Long-wave in-plane buckling of elastoplastic square honeycombs. Int. J. Plast. 22, 1569–1585.

Flory, P.J., Rehner, J., 1943. Statistical mechanics of cross-linked polymer networks II swelling. J. Chem. Phys. 11, 521–526.

Gupta, S., Carrillo, F., Li, C., Pruitt, L., Puttlitz, C., 2007. Adhesive forces significantly affect elastic modulus determination of soft polymeric materials in nanoindentation. Mater. Lett. 61, 448–451.

Guvendiren, M., Burdick, J.A., Yang, S., 2010. Solvent induced transition from wrinkles to creases in thin film gels with depth-wise crosslinking gradients. Soft Matter 6, 5795–5801.

Guvendiren, M., Yang, S., Burdick, J.A., 2009. Swelling-induced surface patterns in hydrogels with gradient crosslinking density. Adv. Funct. Mater. 19, 3038–3045.

Hirth, J.P., Lothe, J., 1982. Theory of Dislocations, Second edition. John Wiley & Sons.

Hong, W., Liu, Z.S., Suo, Z., 2009. Inhomogeneous swelling of a gel in equilibrium with a solvent and mechanical load. Int. J. Solids Struct. 46, 3282–3289.

Hong, W., Zhao, X.H., Zhou, J.X., Suo, Z., 2008. A theory of coupled diffusion and large deformation in polymeric gels. J. Mech. Phys. Solids 56, 1779–1793.

Huggins, M.L., 1964. A revised theory of high polymer solutions. J. Chem. Phys. 86, 3535–3540.

Jang, J.H., Koh, C.Y., Bertoldi, K., Boyce, M.C., Thomas, E.L., 2009. Combining pattern instability and shape-memory hysteresis for phononic switching. Nano Lett. 9, 2113–2119.

Kang, M.K., Huang, R., 2010a. A variational approach and finite element implementation for swelling of polymeric hydrogels under geometric constraints. J. Appl. Mech. 77, 061004.

Kang, M.K., Huang, R., 2010b. Swell-induced surface instability of confined hydrogel layers on substrates. J. Mech. Phys. Solids 58, 1582–1598.

Lee, J.N., Park, C., Whitesides, G.M., 2003. Solvent compatibility of poly (dimethylsiloxane)-based microfluidic devices. Anal. Chem. 75, 6544–6554.

Li, B., Cao, Y.P., Feng, X.Q., Gao, H., 2012. Mechanics of morphological instabilities and surface wrinkling in soft materials: a review. Soft Matter 8, 5728–5745.

Matsumoto, E.A., Kamien, R.D., 2009. Elastic-instability triggered pattern formation. Phys. Rev. E 80, 021604.

Ohno, N., Okumura, D., Niikawa, T., 2004. Long-wave buckling of elastic square honeycombs subject to in-plane biaxial compression. Int. J. Mech. Sci. 46, 1697–1713.

Ohno, N., Okumura, D., Noguchi, H., 2002. Microscopic symmetric bifurcation condition cellular solids based on a homogenization theory of finite deformation. J. Mech. Phys. Solids 50, 1125–1153.

Okumura, D., Kuwayama, T., Ohno, N., 2014. Effect of geometrical imperfections on swelling-induced buckling patterns in gel films with a square lattice of holes. Int. J. Solids Struct. 51, 154–163.

Okumura, D., Ohno, N., Noguchi, H., 2002. Post-buckling analysis of elastic honeycombs subject to in-plane biaxial compression. Int. J. Solids Struct. 39, 3487–3503.

Okumura, D., Ohno, N., Noguchi, H., 2004. Elastoplastic microscopic bifurcation and post-bifurcation behavior of periodic cellular solids. J. Mech. Phys. Solids 52, 641–666.

Petri, H.M., Schuld, N., Wolf, B.A., 1995. Hitherto ignored effects of chain length on the Flory-Huggins interaction parameters in concentrated polymer solutions. Macromolecules 28, 4975–4980.

Roca-Cusachs, P., Rico, F., Martinez, E., Toset, J., Farre, R., Navajas, D., 2005. Stability of microfabricated high aspect ratio structures in poly(dimethylsiloxane). Langmuir 21, 5542–5548.

Singamaneni, S., Bertoldi, K., Chang, S., Jang, J.H., Young, S.L., Thomas, E.L., Boyce, M.C., Tsukruk, V.V., 2009. Bifurcated mechanical behavior of deformed periodic porous solids. Adv. Funct. Mater. 19, 1426–1436.

Tanaka, T., Sun, S-.T., Hirokawa, Y., Katayama, S., Kucera, J., Hirose, Y., Amiya, T.,

1987. Mechanical instability of gels at the phase transition. Nature 325, 796–798.

Toh, W., Liu, Z.S., Ng, T.Y., Hong, W., 2013. Inhomogeneous large deformation kinetics of polymeric gels. Int. J. Appl. Mech. 5, 1350001.

Treloar, L.R.G., 1975. The Physics of Rubber Elasticity. Oxford University Press, Oxford.

Wu, Z., Bouklas, N., Huang, R., 2013. Swell-induced surface instability of hydrogel layers with material properties varying in thickness direction. Int. J. Solids Struct. 50, 578–587.

Yang, S., Khare, K., Lin, P.C., 2010. Harnessing surface wrinkle patterns in soft matter. Adv. Funct. Mater. 20, 2550–2564.

Zhang, Y., Matsumoto, E.A., Peter, A., Lin, P.C., Kamien, R.D., Yang, S., 2008. One-step nanoscale assembly of complex structures via harnessing of an elastic instability. Nano Lett. 8, 1192–1196.

Zhang, Y., Reed, J.C., Yang, S., 2009. Creating a library of complex metallic nanostructures via harnessing pattern transformation of a single PDMS membrane. ACS Nano 3, 2412–2418.

Zhu, X., Wu, G., Dong, R., Chen, C.M., Yang, S., 2012. Capillarity induced instability in responsive hydrogel membranes with periodic hole array. Soft Matter 8, 8088–8093.

Legends to Figures

Fig. 1. Schematic diagrams showing a polymeric film with a square lattice of holes being pre-strained in uniaxial tension in a lattice direction and subsequently swelled by a solvent.

Fig. 2. Initial configuration and finite element meshes; (a) 10×10 unit cell with random imperfections and (b) 2×2 unit cell with a simple imperfection.

Fig. 3. Macroscopic stress–strain relationships for prestrains of $\varepsilon=0$, 0.2, 0.4 and 0.6 (10×10 unit cell).

Fig. 4. Macroscopic stress as a function of the average deviation from roundness for prestrains of $\varepsilon=0$, 0.2, 0.4 and 0.6 (10×10 unit cell).

Fig. 5. Deformed configurations and normalized concentration distributions υC for prestrain of $\varepsilon=0$ (10×10 unit cell); (a), (b) and (c) at states (i), (ii) and (iii) in Fig. 4.

Fig. 6. Deformed configurations and normalized concentration distributions υC for prestrain of $\varepsilon=0.2$ (10×10 unit cell); (a), (b) and (c) at states (i), (ii) and (iii) in Fig. 4.

Fig. 7. Deformed configurations and normalized concentration distributions υC for prestrain of $\varepsilon=0.4$ (10×10 unit cell); (a) and (b) at states (i) and (ii) in Fig. 4.

Fig. 8. Deformed configurations and normalized concentration distributions υC for prestrain of $\varepsilon=0.6$ (10×10 unit cell); (a) and (b) at states (i) and (ii) in Fig. 4.

Fig. 9. Macroscopic stress as a function of the deviations from roundness of individual holes (2×2 unit cell); (a)–(d) for prestrains of $\varepsilon=0$, 0.2, 0.4 and 0.6.

Fig. 10. Deformed configurations and normalized concentration distributions υC (2×2 unit cell); (a)–(d) for prestrains of $\varepsilon=0$, 0.2, 0.4 and 0.6 at states (i)–(iv) in Fig. 9.

Fig. 11. Macroscopic stress as a function of the external chemical potential μ (2×2

unit cell); (a) from a quasi-dry state to equilibrium swelling and (b) near equilibrium swelling.

Fig. 12. Deformed configurations and normalized concentration distributions υC at equilibrium swelling for Cases 1–3 (2×2 unit cell).

Fig. 13. Dependence of the resulting patterns at equilibrium swelling on the swelling ratio at quasi-dry state of λ_0 =1.001, 1.01 and 1.1 (2×2 unit cell).

Fig. 14. Influence of dissipated energy fraction ω on the maximum stress for prestrains of $\varepsilon=0$, 0.2, 0.4 and 0.6 (2×2 unit cell).

Figure01

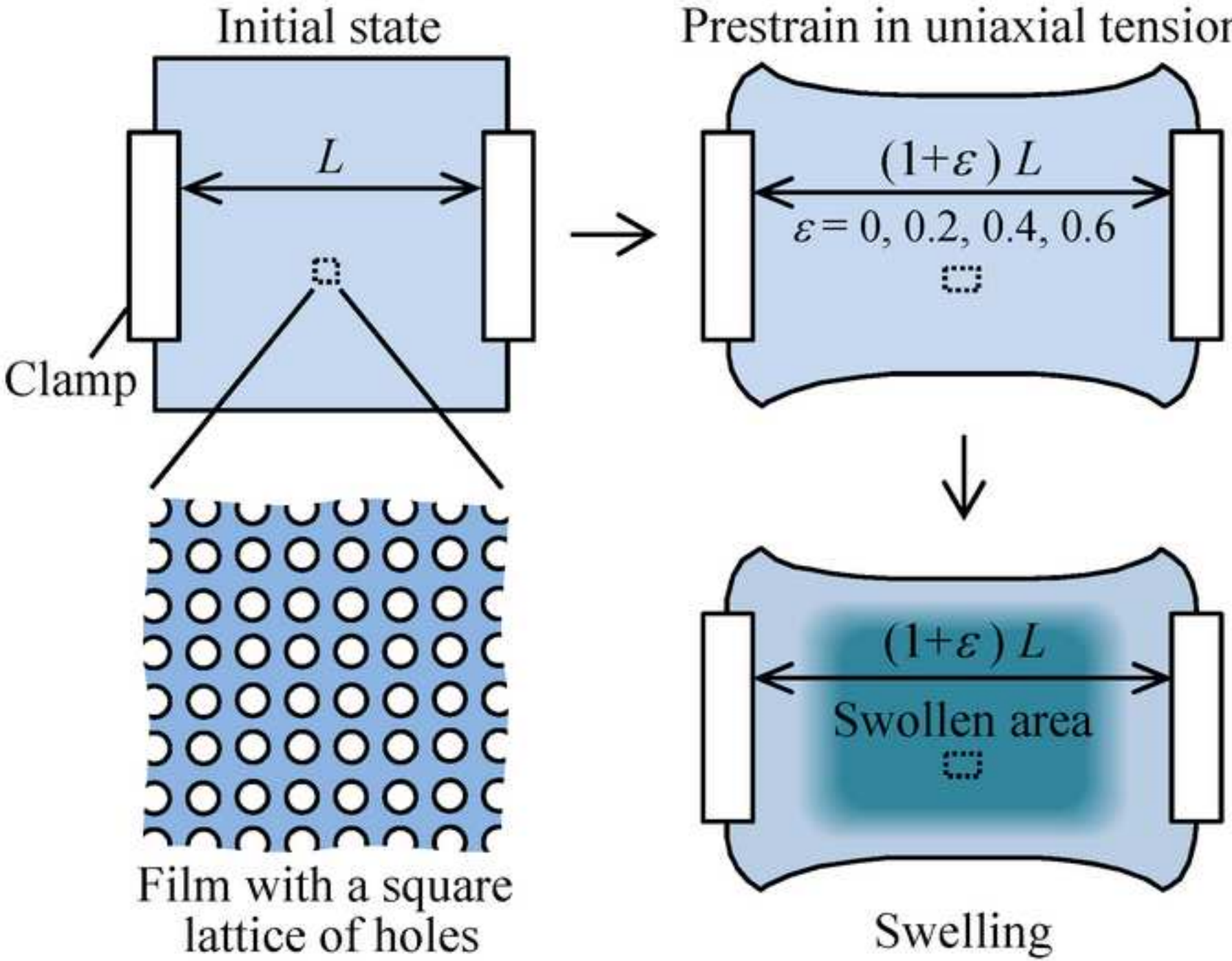

Figure02

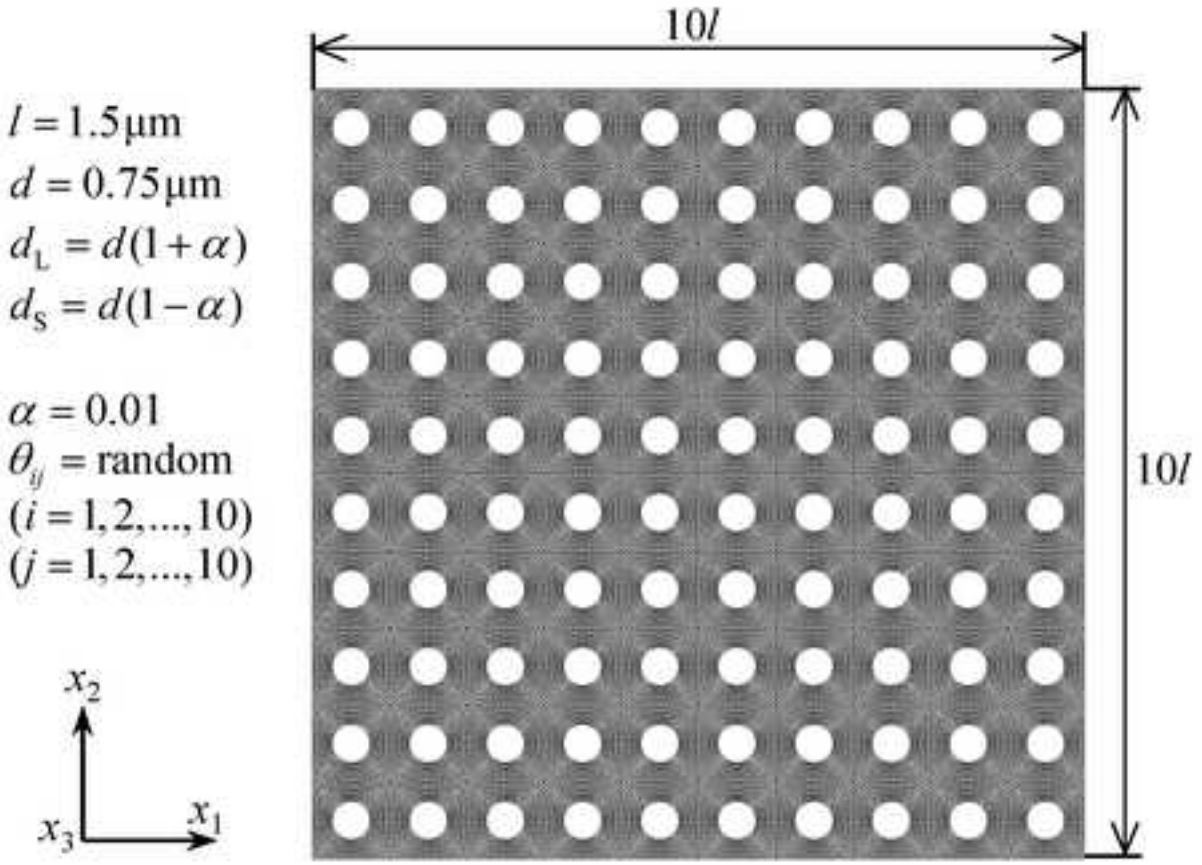

(a) 10×10 unit cell

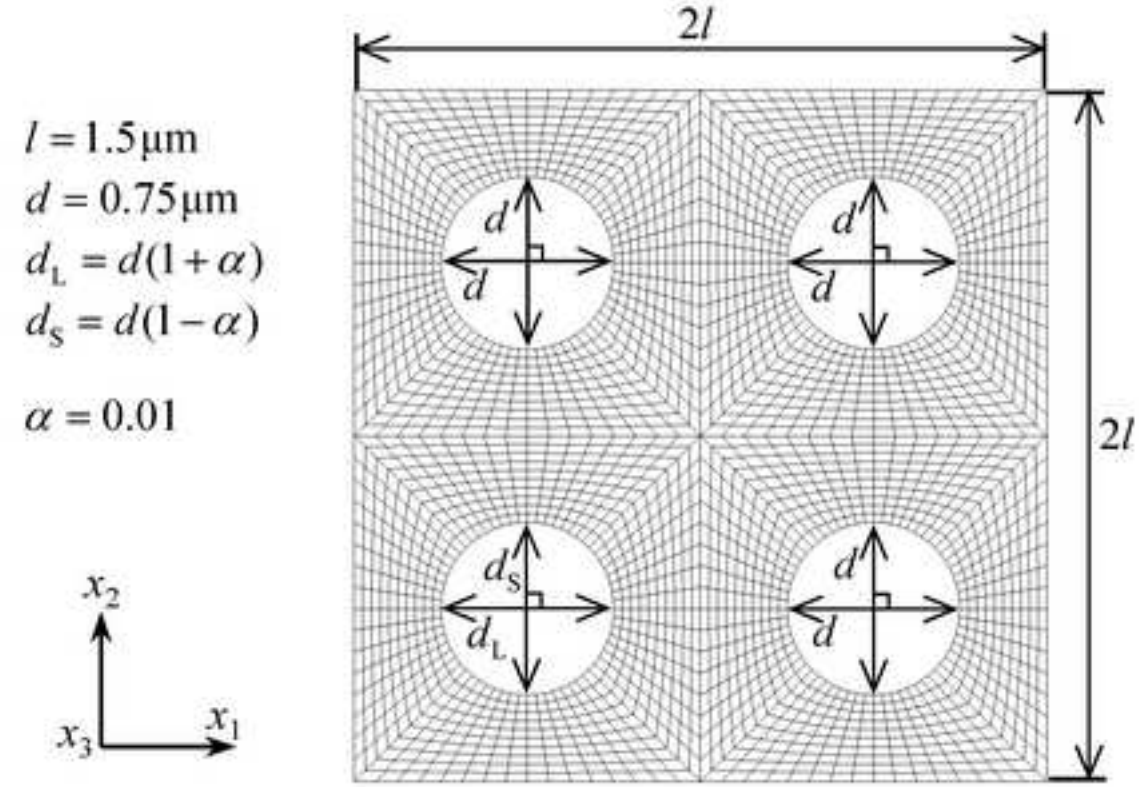

(b) 2×2 unit cell

Figure03

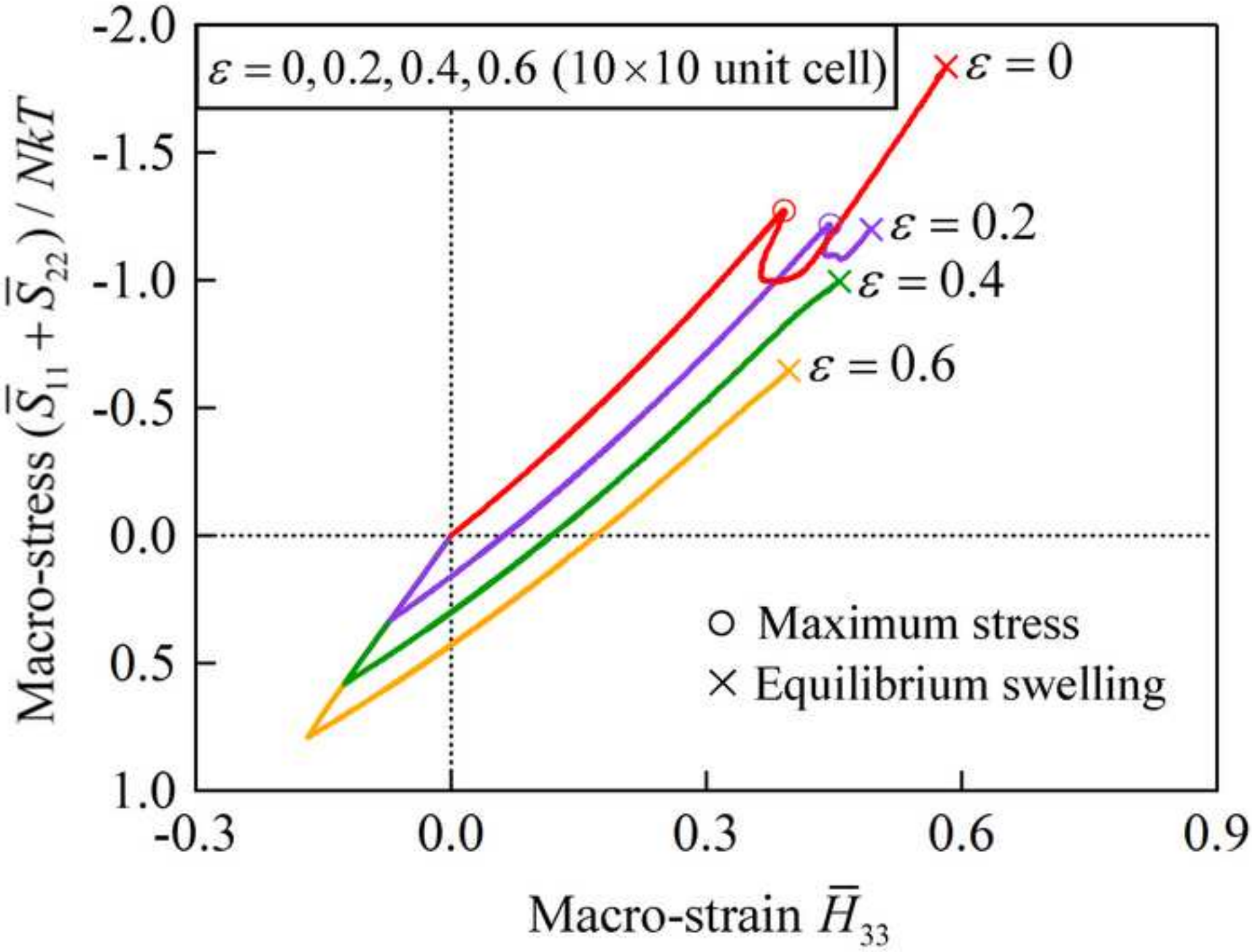

Figure04

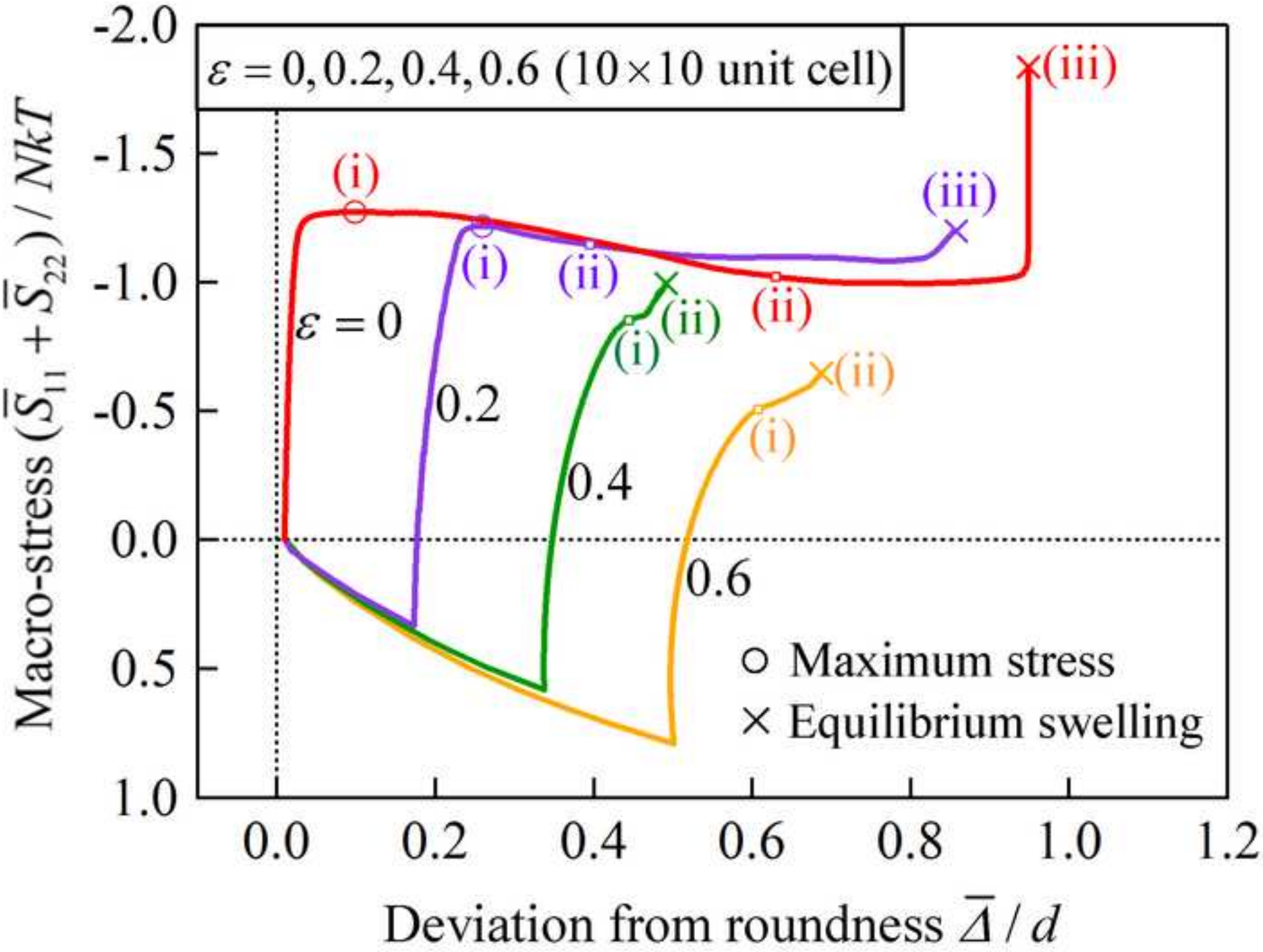

Figure05

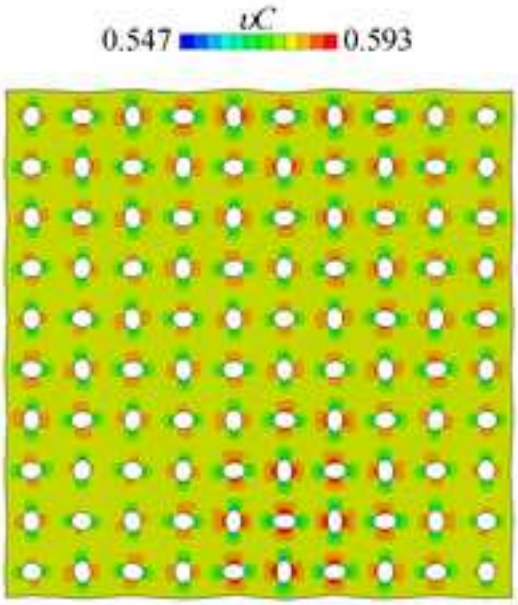

(a) State (i)

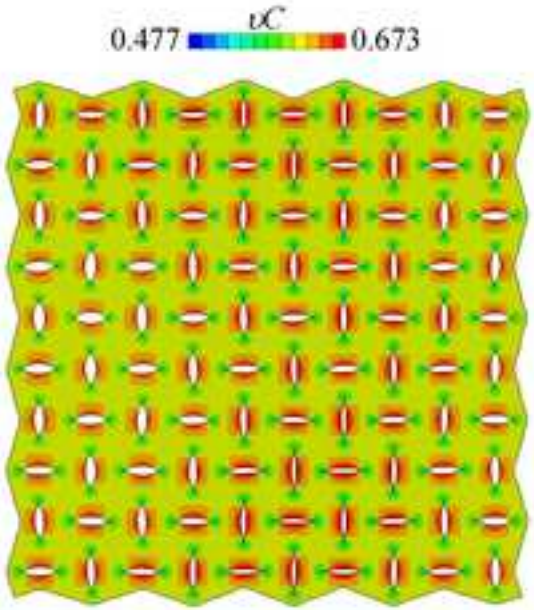

(b) State (ii)

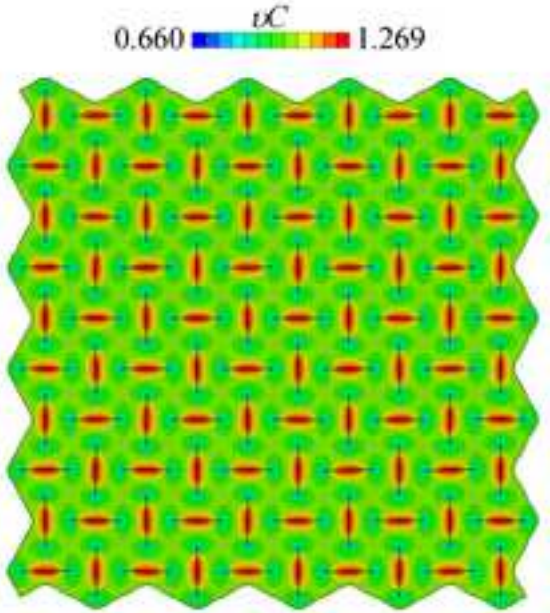

(c) State (iii)

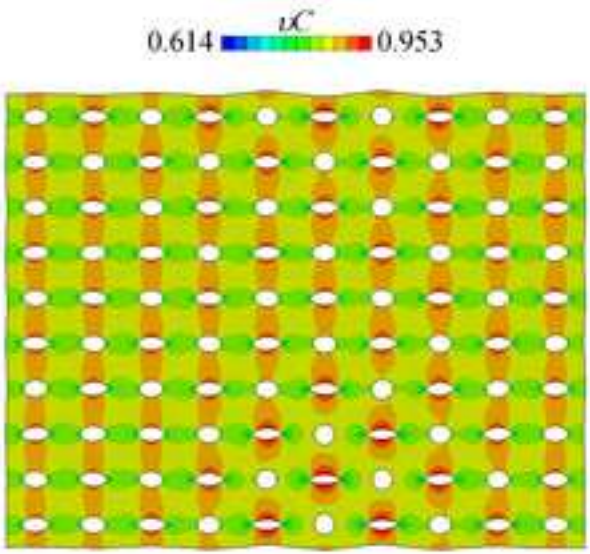

(a) State (i)

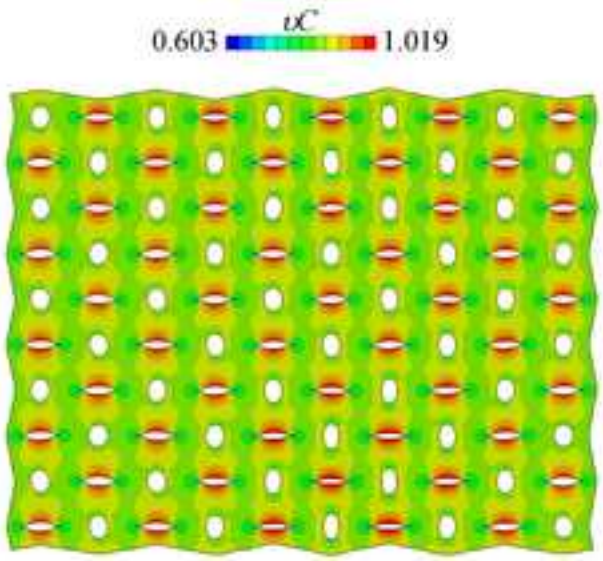

(b) State (ii)

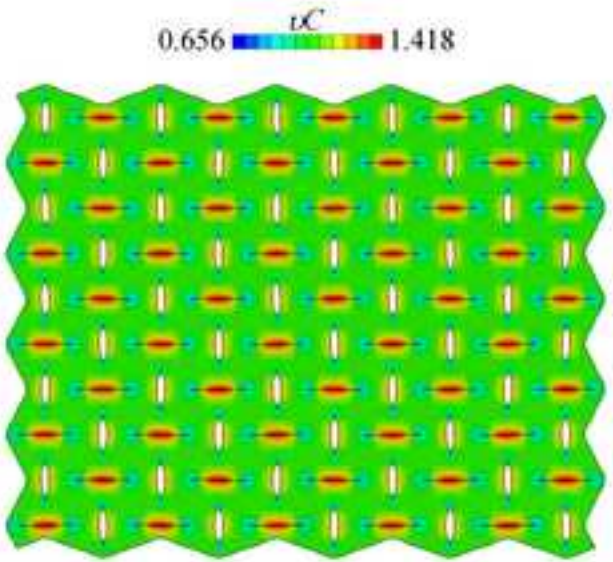

(c) State (iii)

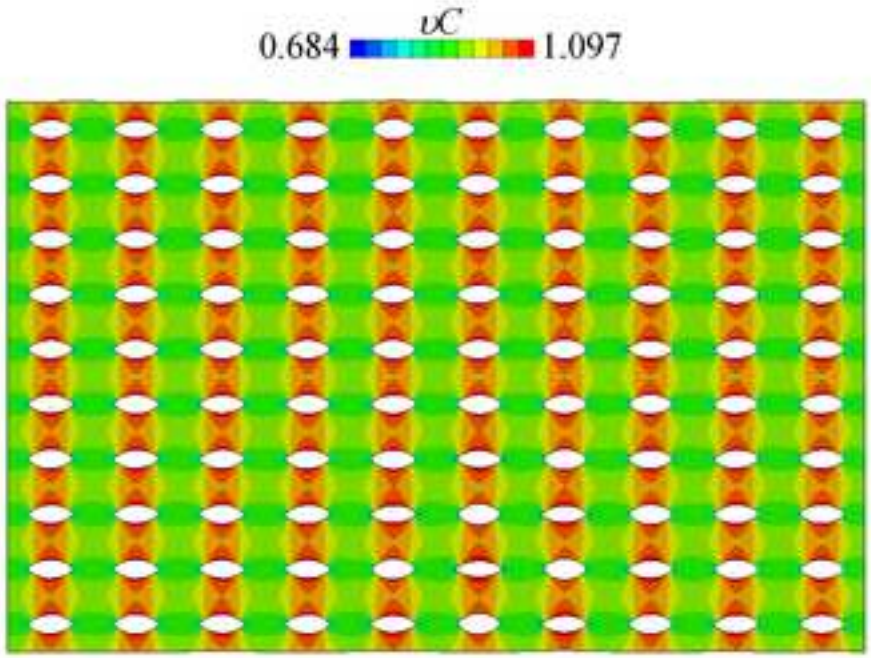

(a) State (i)

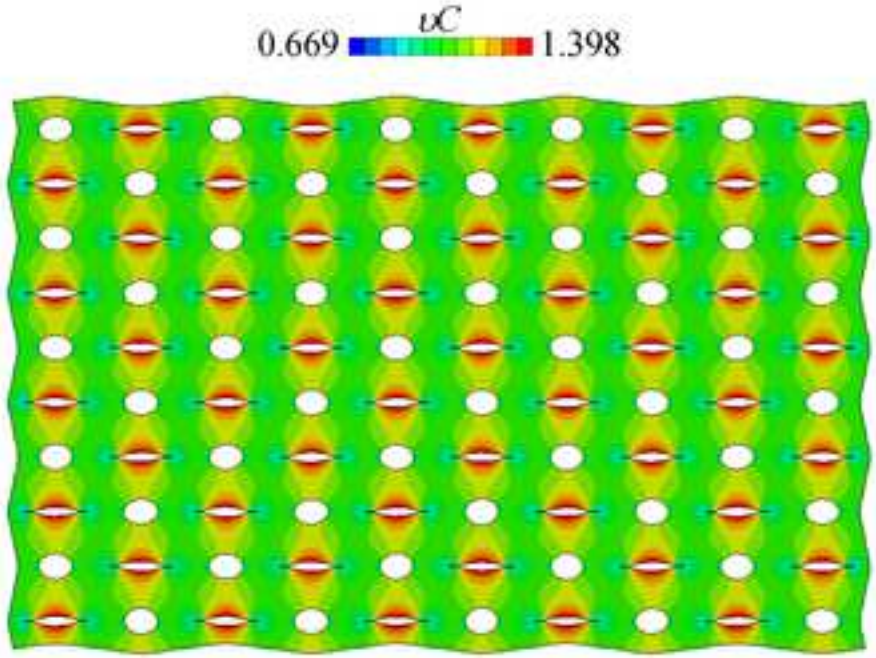

(b) State (ii)

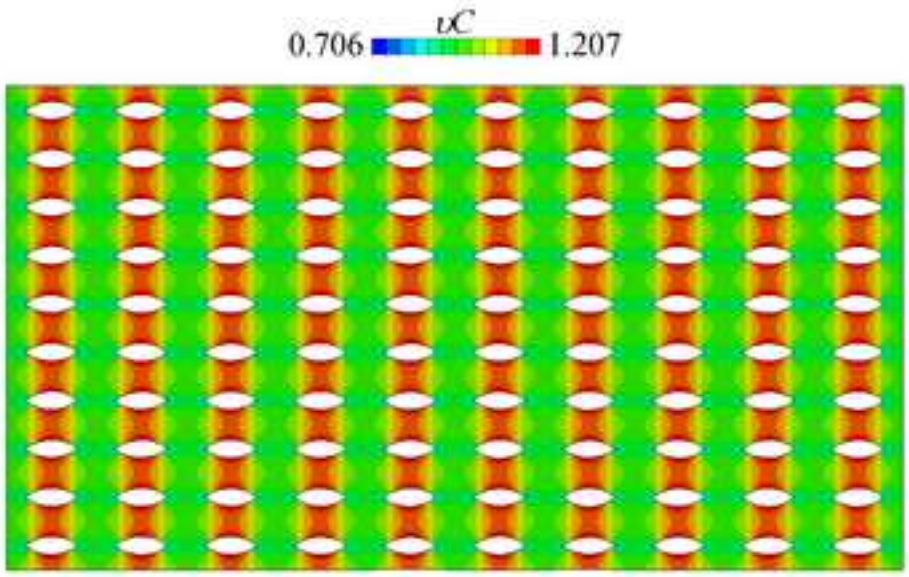

(a) State (i)

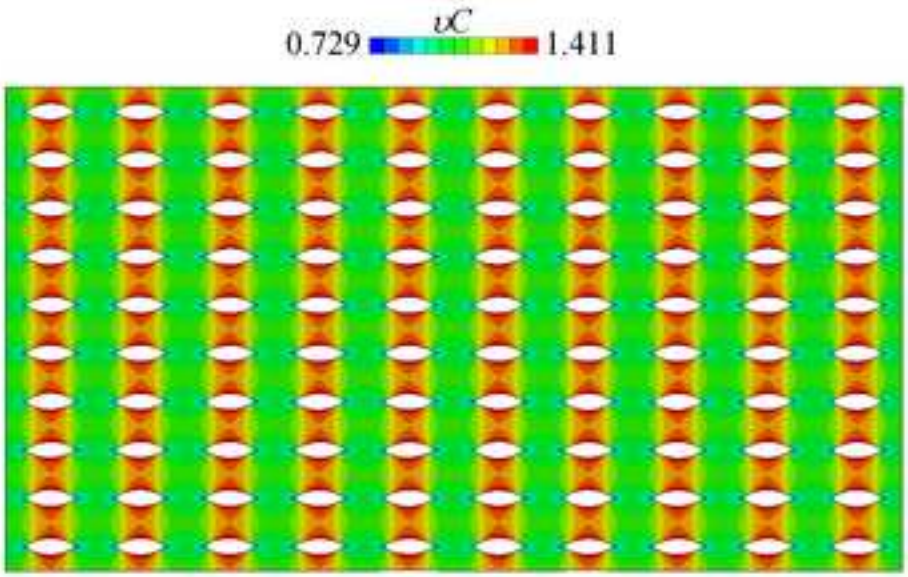

(b) State (ii)

Figure09

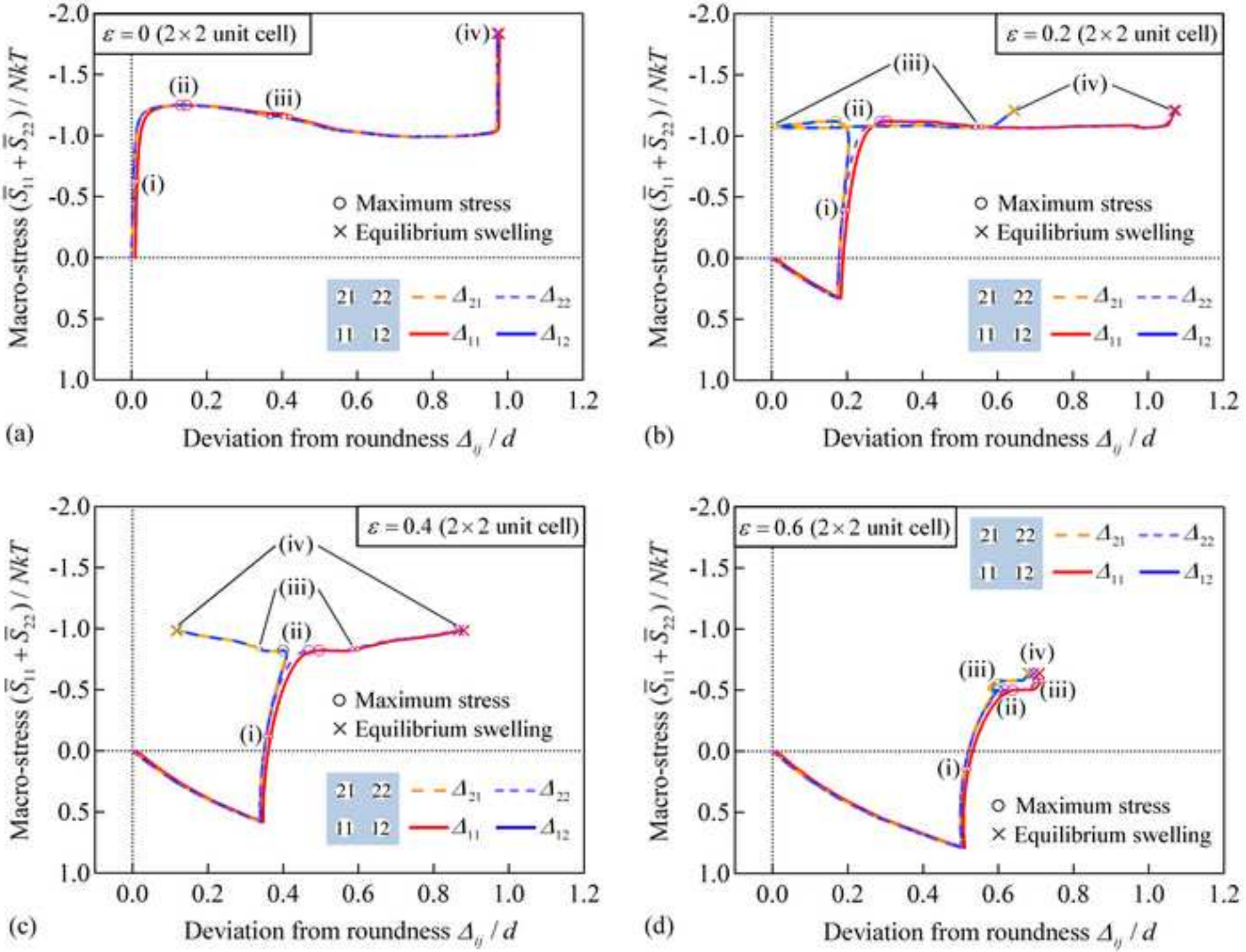

Figure10

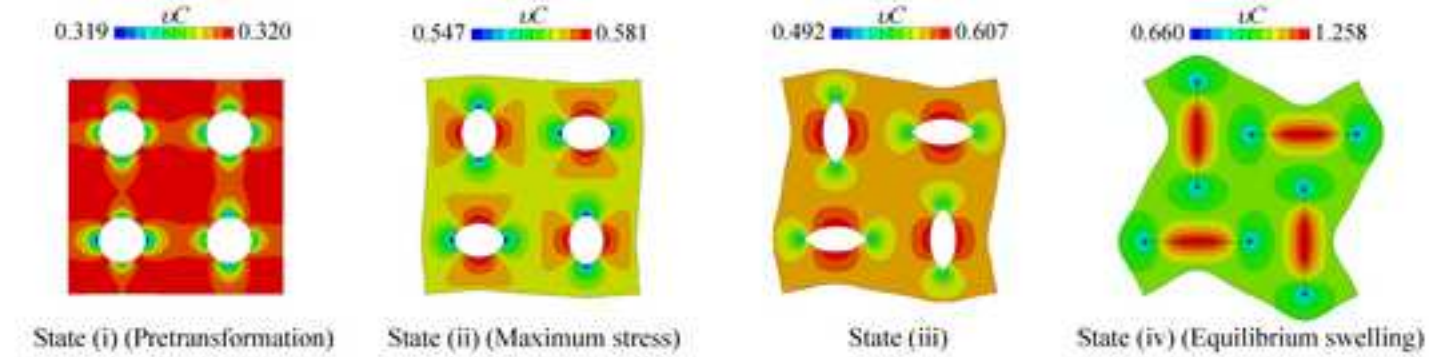

State (i) (Pretransformation) State (ii) (Maximum stress) State (iii) State (iv) (Equilibrium swelling)

(a) Prestrain $\varepsilon = 0$

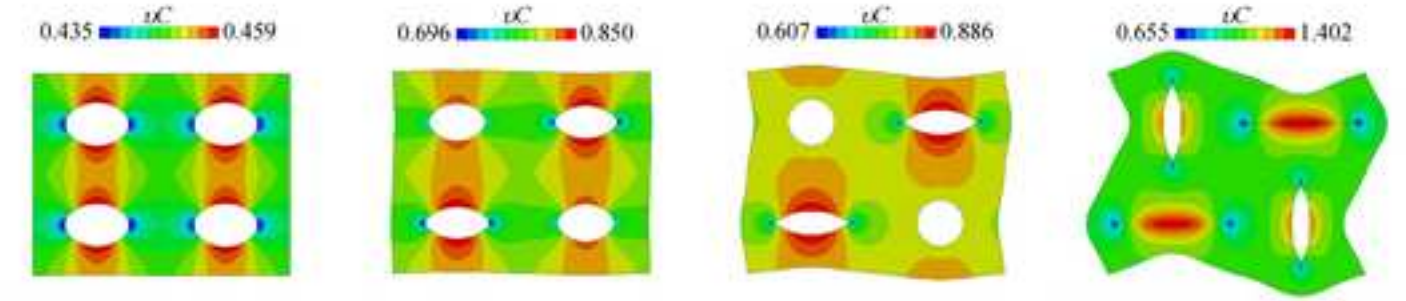

State (i) (Pretransformation) State (ii) (Maximum stress) State (iii) State (iv) (Equilibrium swelling)

(b) Prestrain $\varepsilon = 0.2$

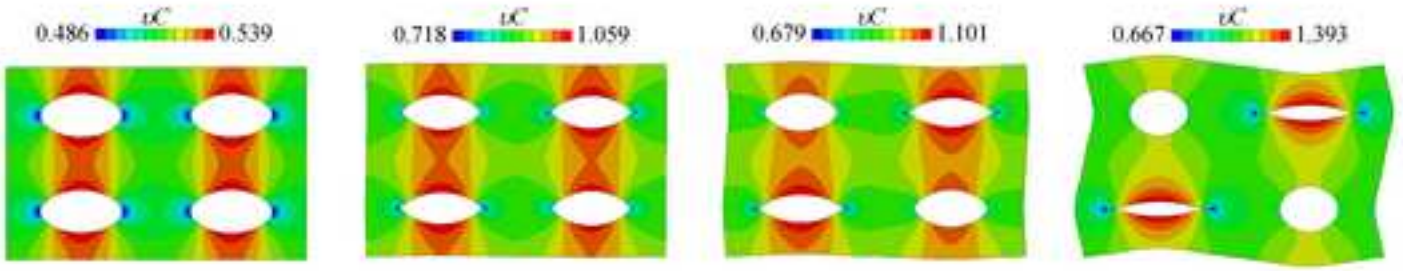

State (i) (Pretransformation) State (ii) (Maximum stress) State (iii) State (iv) (Equilibrium swelling)

(c) Prestrain $\varepsilon = 0.4$

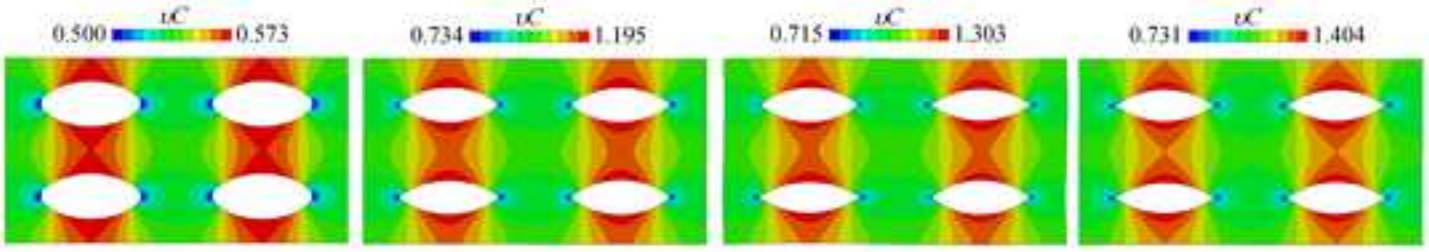

State (i) (Pretransformation) State (ii) (Maximum stress) State (iii) State (iv) (Equilibrium swelling)

(d) Prestrain $\varepsilon = 0.6$

Figure11

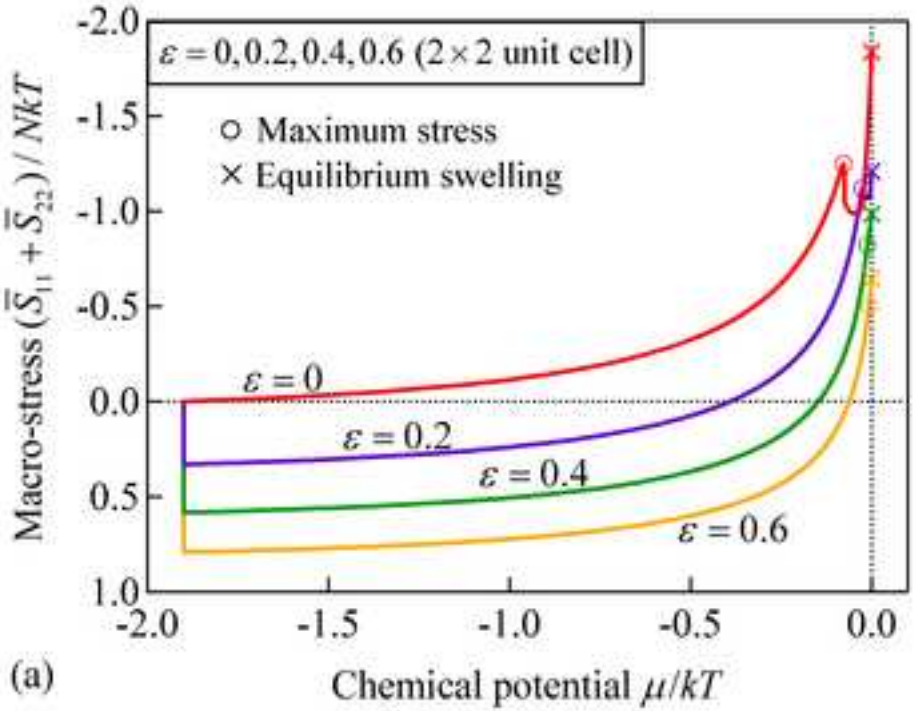

(a)

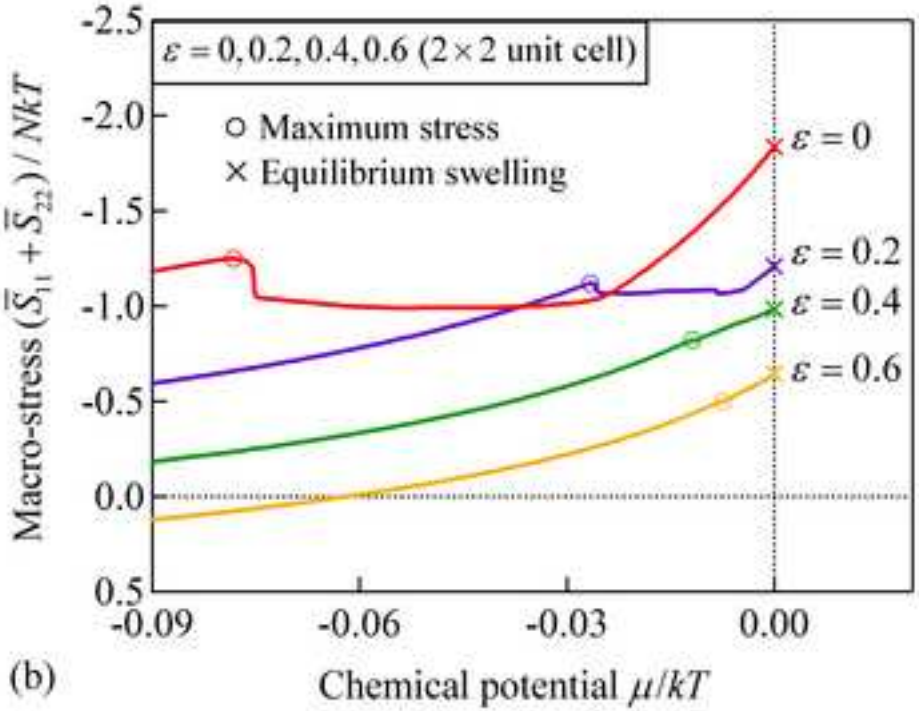

(b)

Figure12

Prestrains	$\varepsilon = 0$	$\varepsilon = 0.2$	$\varepsilon = 0.4$	$\varepsilon = 0.6$
Case 1 $E = 2.0$ MPa $\chi = 0.8$	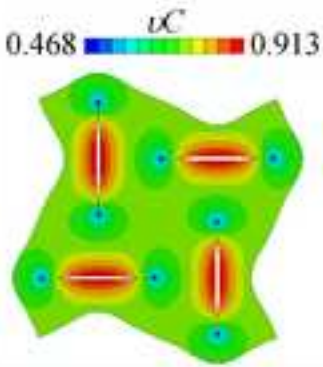	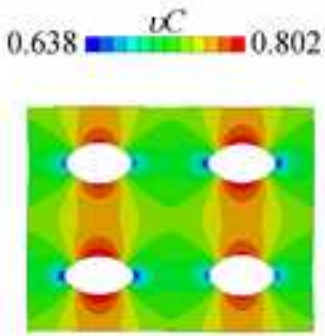	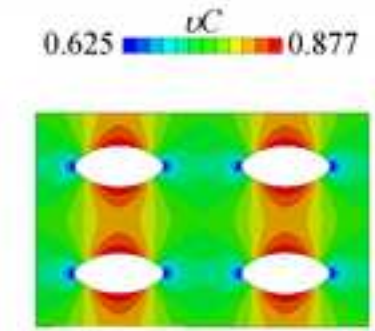	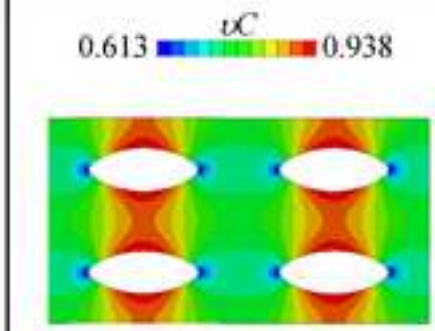
Case 2 $E = 1.5$ MPa $\chi = 0.7$	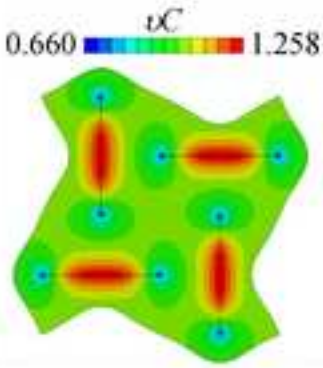	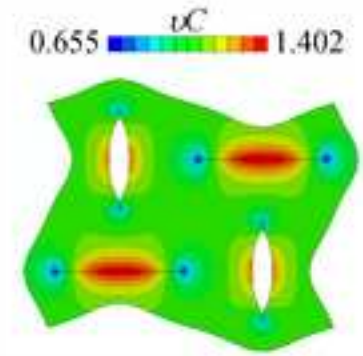	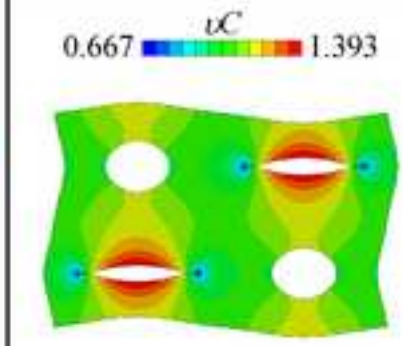	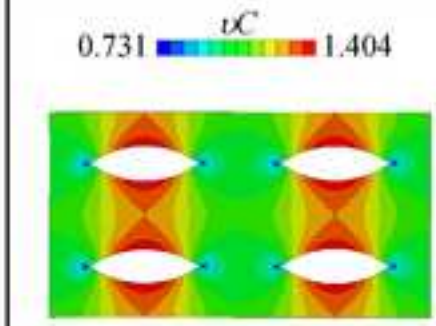
Case 3 $E = 1.0$ MPa $\chi = 0.6$	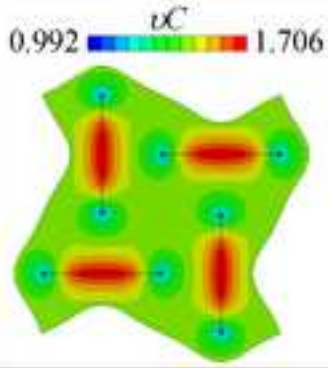	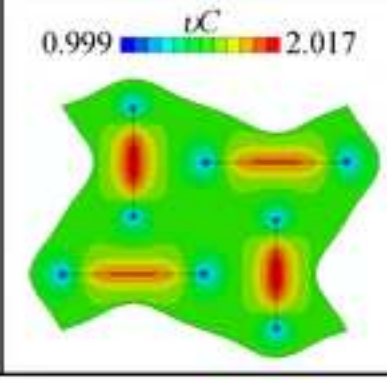	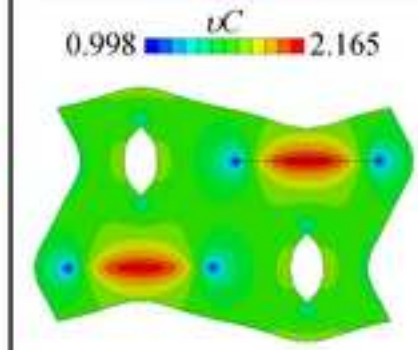	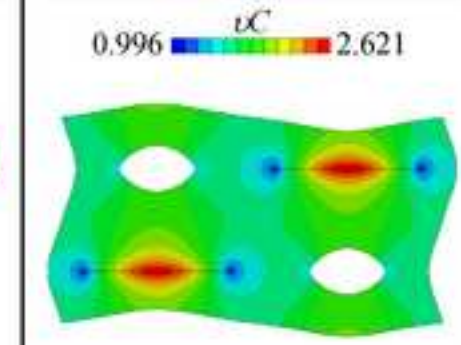

Figure13

Prestrains	$\varepsilon = 0$	$\varepsilon = 0.2$	$\varepsilon = 0.4$	$\varepsilon = 0.6$
$\lambda_0 = 1.001$ $E = 1.5$ MPa $\chi = 0.7$	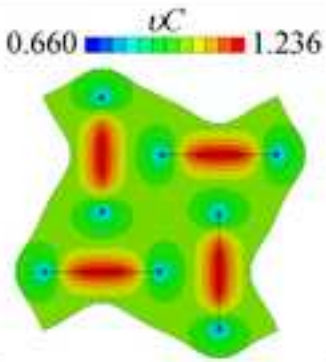	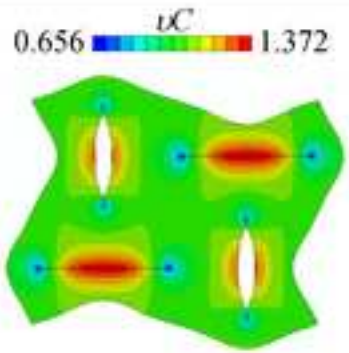	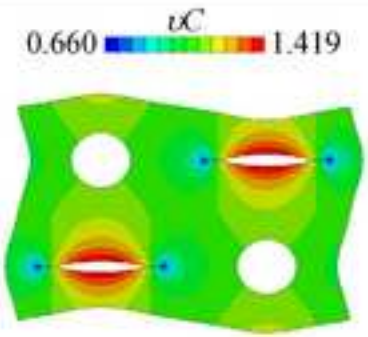	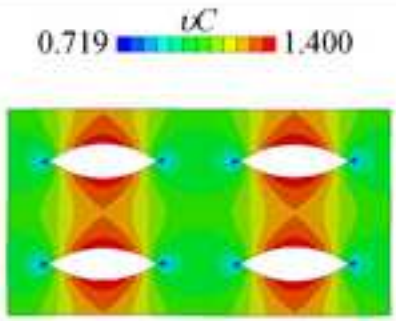
$\lambda_0 = 1.01$ $E = 1.5$ MPa $\chi = 0.7$	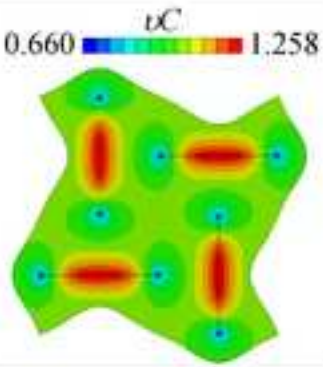	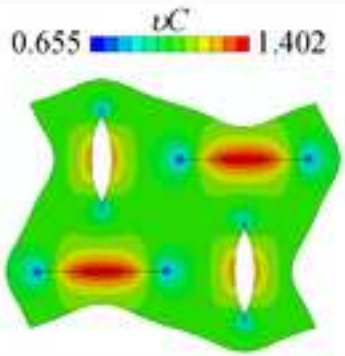	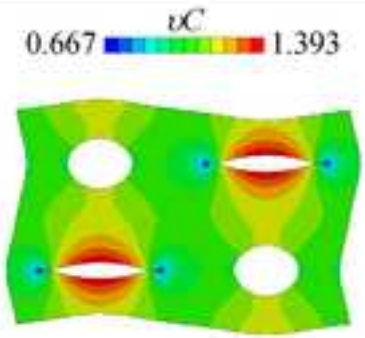	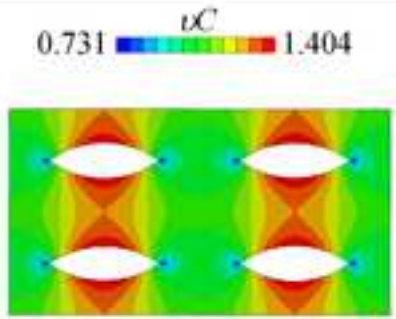
$\lambda_0 = 1.1$ $E = 1.5$ MPa $\chi = 0.7$	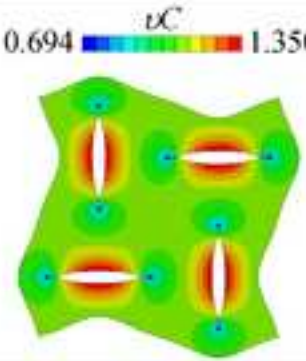	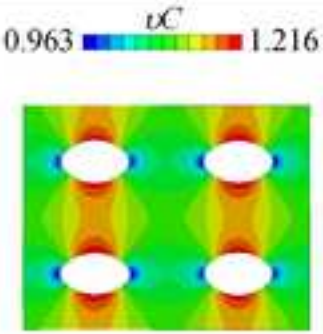	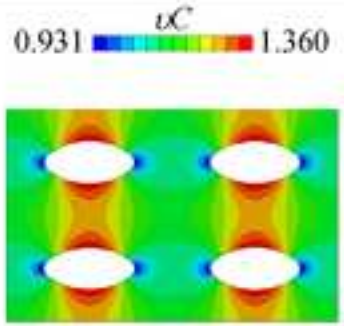	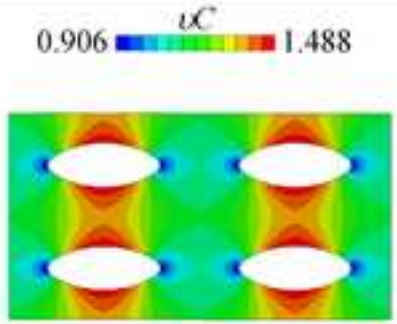

Figure14